The Astrophysical Journal, 931:137 (22pp), 2022 June 1 https://doi.org/10.3847/1538-4357/ac6acd

Kinetic Simulations of Instabilities and Particle Acceleration in Cylindrical Magnetized Relativistic Jets

José Ortuño-Macías[1], Krzysztof Nalewajko[1], Dmitri A. Uzdensky[2], Mitchell C. Begelman[3,4], Gregory R. Werner[2], Alexander Y. Chen[3], and Bhupendra Mishra[5]
[1] Nicolaus Copernicus Astronomical Center, Polish Academy of Sciences, Bartycka 18, 00-716 Warsaw, Poland; jortuno@camk.edu.pl, knalew@camk.edu.pl
[2] Center for Integrated Plasma Studies, Department of Physics, University of Colorado, 390 UCB, Boulder, CO 80309-0390, USA
[3] JILA, University of Colorado and National Institute of Standards and Technology, 440 UCB, Boulder, CO 80309-0440, USA
[4] Department of Astrophysical and Planetary Sciences, University of Colorado, 391 UCB, Boulder, CO 80309, USA
[5] Los Alamos National Laboratory, Los Alamos, NM 87545, USA
Received 2022 February 9; revised 2022 April 12; accepted 2022 April 25; published 2022 June 3

Abstract

Relativistic magnetized jets, such as those from AGN, GRBs, and XRBs, are susceptible to current- and pressure-driven MHD instabilities that can lead to particle acceleration and nonthermal radiation. Here, we investigate the development of these instabilities through 3D kinetic simulations of cylindrically symmetric equilibria involving toroidal magnetic fields with electron–positron pair plasma. Generalizing recent treatments by Alves et al. and Davelaar et al., we consider a range of initial structures in which the force due to toroidal magnetic field is balanced by a combination of forces due to axial magnetic field and gas pressure. We argue that the particle energy limit identified by Alves et al. is due to the finite duration of the fast magnetic dissipation phase. We find a rather minor role of electric fields parallel to the local magnetic fields in particle acceleration. In all investigated cases, a kink mode arises in the central core region with a growth timescale consistent with the predictions of linearized MHD models. In the case of a gas-pressure-balanced (Z-pinch) profile, we identify a weak local pinch mode well outside the jet core. We argue that pressure-driven modes are important for relativistic jets, in regions where sufficient gas pressure is produced by other dissipation mechanisms.

Unified Astronomy Thesaurus concepts: High energy astrophysics (739); Jets (870)

1. Introduction

Magnetic fields are thought to play a decisive role in many of the most energetic astrophysical phenomena. Compact accreting objects tend to accumulate (or generate locally) magnetic fields and sort them out from the matter (e.g., Narayan et al. 2003). This can produce extreme environments in which the magnetic energy density locally dominates the rest-mass density of matter. Such relativistic magnetizations can be converted to high Lorentz factors, driving relativistic outflows in the form of collimated jets (e.g., Begelman et al. 1984; Li et al. 1992; Begelman & Li 1994; Beskin & Nokhrina 2006; Komissarov et al. 2007; Tchekhovskoy et al. 2009). Luminous nonthermal emission with photon energies extending into the gamma-ray band is a key observational signature of such environments (e.g., Tavani et al. 2011; Abdo et al. 2011; Madejski & Sikora 2016); it is evidence of efficient nonthermal acceleration of particles to ultrarelativistic energies. A likely mechanism for particle acceleration in such environments is relativistic magnetic reconnection (e.g., Michel 1971; Romanova & Lovelace 1992; Lyubarskii 1996; Drenkhahn & Spruit 2002; Kirk 2004; Uzdensky et al. 2011; Sironi et al. 2015; Werner et al. 2016, 2018; Werner & Uzdensky 2021), developing from large gradients or reversals in the magnetic field. Dissipation of magnetic energy depends crucially on the magnetic topology and the stability of the plasma configuration.

Axially symmetric magnetic field configurations may involve ordered poloidal and toroidal components. As they expand over several orders of magnitude in distance, the poloidal component decays faster than the toroidal component. Even if the configurations are initially dominated by the poloidal component, the toroidal component can in principle become dominant at some point. Toroidal magnetic fields are well-known to be unstable to either current-driven or pressure-driven pinch (sausage) and kink modes (e.g., Kruskal & Schwarzschild 1954; Kadomtsev 1966; Freidberg 1982). These instabilities have been proposed to be the trigger of magnetic dissipation in relativistic jets of active galactic nuclei (AGNs) and gamma-ray bursts (GRBs), and in pulsar wind nebulae (Begelman 1998; Drenkhahn & Spruit 2002; Giannios & Spruit 2006).

Most analytic studies of the stability of relativistic magnetized jets have been performed in cylindrical geometry (e.g., Istomin & Pariev 1994; Begelman 1998; Lyubarskii 1999; Appl et al. 2000; Tomimatsu et al. 2001; Nalewajko & Begelman 2012; Bodo et al. 2013; Das & Begelman 2019; Bodo et al. 2019).[6] This allows one to introduce a cylindrical coordinate system (r, ϕ, z), in which all equilibrium parameters depend solely on r. Various assumptions have been adopted on the radial profile of the toroidal magnetic field $B_\phi(r)$, the presence of the axial (poloidal) magnetic field $B_z(r)$, and crucially on the radial force balance, which may involve contributions from the magnetic field, gas pressure, centrifugal force, and radial shear of the axial velocity.

One line of research has been to adopt the force-free (FF) approximation, in which contributions from the gas pressure or inertia are neglected, and the $(\boldsymbol{j} \times \boldsymbol{B})/c$ force density due to

[6] However, the effects of jet collimation can be important (e.g., Narayan et al. 2009).

$B_\phi(r)$ is balanced by that due to $B_z(r)$ (the *screw-pinch* configuration). In the FF limit, it has typically been found that the pinch mode (with azimuthal wavenumber $m = 0$) is stable, and that the dominant unstable mode is the *global* (or *external*, with axial wavelength λ_z comparable to the jet radius R_j) $m = 1$ kink mode (e.g., Istomin & Pariev 1994; Lyubarskii 1999; Appl et al. 2000; Bodo et al. 2013).

Another line of research has been to balance the force due to $B_\phi(r)$ with gas pressure gradients, even without any axial magnetic fields ($B_z = 0$). In this *Z-pinch* configuration, the most unstable modes are *internal* (with short axial wavelengths $\lambda_z \ll R_j$). They can also be *local* (localized at large radii as compared with the wavelength $\lambda_z \ll r$), and can be either pinch or kink modes (as the growth rate depends weakly on m) (Begelman 1998; Nalewajko & Begelman 2012; Das & Begelman 2019).

The stability and nonlinear evolution of relativistic jets have been investigated numerically using 3D relativistic MHD (RMHD) simulations. The simplest approach has been to consider a static, cylindrically symmetric column representing the innermost jet region in its comoving frame. Such simulations have been performed in both the FF limit (Mizuno et al. 2009; Bromberg et al. 2019; Mukherjee et al. 2021; Bodo et al. 2022) and the Z-pinch limit (Mizuno et al. 2011a). These two regimes have been compared in the work of O'Neill et al. (2012), which emphasized a dramatically more disruptive outcome of instability in the Z-pinch case, a result well known in fusion plasma physics (e.g., Freidberg 1982). Further studies in the FF regime considered the effects of radial shear of the axial velocity (Mizuno et al. 2011b, 2014) or rotation about the symmetry axis (Mizuno et al. 2012; Singh et al. 2016).

Global 3D MHD and RMHD simulations resulting in the development of current-driven instabilities have been performed for nonrelativistic and relativistic jets in AGNs (Nakamura & Meier 2004; Moll et al. 2008; McKinney & Blandford 2009; Mignone et al. 2010; Tchekhovskoy & Bromberg 2016), gamma-ray bursts (Bromberg & Tchekhovskoy 2016), and pulsar wind nebulae (Mignone et al. 2013; Porth et al. 2014). These simulations demonstrated consistently that the dominant modes are either pinch or kink.

MHD simulations are able to provide limited information about nonthermal particle acceleration, e.g., in the test particle approximation (e.g., Puzzoni et al. 2021). However, in order to fully account for kinetic effects, the particle-in-cell (PIC) algorithm is the method of choice. Recently, the results of the first 3D kinetic collisionless PIC simulations of static cylindrical columns with relativistically strong toroidal magnetic fields in pair plasmas have been reported. In the work of Alves et al. (2018), a radial profile of toroidal magnetic field with an exponentially decaying outer tail was balanced entirely by gas pressure (the Z-pinch or the screw-pinch with uniform axial field B_z), which resulted in internal unstable modes.[7] On the other hand, in the work of Davelaar et al. (2020), toroidal magnetic field with a power-law tail (approximately $B_\phi \propto r^{-1}$) was balanced by a nonuniform axial field B_z in the FF screw-pinch configuration with subrelativistically warm plasma, which resulted in external unstable modes.

Alves et al. (2018, 2019) demonstrated nonthermal particle acceleration associated with pressure-driven modes. They obtained power-law energy distributions $dN/d\gamma \propto \gamma^{-p}$ [8] with the index $p \sim 2$–3. These distributions extended to the maximum energy of $\gamma_{\rm max} \simeq (1.6\text{–}1.9)\gamma_{\rm lim}$, where

$$\gamma_{\rm lim} \equiv \frac{|q|B_0 R_0}{mc^2} \tag{1}$$

is the energy limit[9] (corresponding to the Hillas criterion; Hillas 1984), referred to as the *confinement energy* (see Appendix A). This limit has been tentatively confirmed by Davelaar et al. (2020), who also found power-law particle energy distributions with $p \sim 3$–5 and maximum energy of $\gamma_{\rm max} \simeq \gamma_{\rm lim}/6$.

Both Alves et al. (2018, 2019) and Davelaar et al. (2020) investigated the nature of electric fields accelerating particles in unstable cylindrical jets, using the electric field component $\boldsymbol{E}_\parallel = (\boldsymbol{E}\cdot\boldsymbol{B})\boldsymbol{B}/B^2$ parallel to the local magnetic field $\boldsymbol{B}$ as a proxy for the nonideal electric field component $\boldsymbol{E}_{\rm nonid} = \boldsymbol{E} - \boldsymbol{B}\times\boldsymbol{\beta}_{\rm b}$, where $\boldsymbol{\beta}_{\rm b} = \boldsymbol{v}_{\rm b}/c$ is the bulk velocity $\boldsymbol{v}_{\rm b}$ in units of c. In the gas-pressure-balanced configurations investigated by Alves et al. (2018, 2019), perpendicular electric fields $\boldsymbol{E}_\perp = \boldsymbol{E} - \boldsymbol{E}_\parallel$ dominate particle acceleration. On the other hand, in the $B_z(r)$-supported FF configurations investigated by Davelaar et al. (2020), it has been argued that both perpendicular and parallel fields contribute to particle acceleration, the latter due to finite-guide-field reconnection.

In this work, we introduce a new radial profile of toroidal magnetic field that approximates a power law, $B_\phi(r) \propto r^{\alpha_{\rm B}\phi}$, with the toroidal field index $\alpha_{\rm B}\phi \leqslant 0$. The force due to $B_\phi(r)$ is balanced initially by combinations of forces due to axial magnetic field and gas pressure, using a single pressure mixing parameter $f_{\rm mix}$ to transition between the FF screw-pinch configuration with no gas pressure gradients ($f_{\rm mix} = 0$) and the Z-pinch configuration with $B_z = 0$ ($f_{\rm mix} = 1$). We perform a series of 3D kinetic PIC simulations of relativistic collisionless pair plasmas using this setup on a regular Cartesian grid with periodic boundaries. We investigate the effects of the key parameters $f_{\rm mix}$ and $\alpha_{\rm B}\phi$ on the development of instabilities and the resulting particle acceleration.

Section 2 describes the initial configuration used in our simulations. The presentation of our results begins from introducing basic details on our reference simulation in Section 3. Section 4 presents the results at the fluid level focused on the instability modes. In Section 4.1, we compare the strengths and linear growth timescales of the fundamental azimuthal modes in the distributions of the axial electric field component E_z. In Section 4.2, we compare the effective axial wavelengths of the E_z distributions. Section 5 presents the results at the kinetic level, with a focus on the particle acceleration. In Section 5.1, we investigate the maximum energies achieved by particles in our simulations. In Section 5.2, we investigate the role of parallel electric fields in particle acceleration. Section 6 contains a discussion of our results, and Section 7 provides our conclusions.

[7] A related work by Alves et al. (2019) investigated the same magnetic configuration in nonrelativistic electron-ion plasmas, in some cases including the effect of Coulomb collisions.

[8] Here, $\gamma = (1-\beta^2)^{-1/2} = \mathcal{E}/mc^2$ is the Lorentz factor of a particle with mass m, energy $\mathcal{E}$, and dimensionless velocity $\boldsymbol{\beta} = \boldsymbol{v}/c$, with c being the speed of light.

[9] Here, q is the particle electric charge, and B_0 is roughly the peak value of $B_\phi(r)$ attained at the characteristic radius R_0.

2. Initial Configuration

We performed a set of 3D kinetic PIC simulations in electron–positron pair plasma, using a modified version of the public numerical code `Zeltron` (Cerutti et al. 2013).

In our standard collisionless implementation of the PIC method, the electric and magnetic fields $\boldsymbol{E}, \boldsymbol{B}$ are represented on a staggered Cartesian Yee grid, and the gas is represented by individual macroparticles, from which a current density field $\boldsymbol{j}$ is calculated and deposited on the Yee grid using the charge-conserving scheme of Esirkepov (2001). The $\boldsymbol{E}$, $\boldsymbol{B}$ fields are advanced in time by solving directly the Ampère–Maxwell and Maxwell–Faraday equations:

$$\frac{\partial \boldsymbol{E}}{\partial t} = c\boldsymbol{\nabla} \times \boldsymbol{B} - 4\pi \boldsymbol{j}, \tag{2}$$

$$\frac{\partial \boldsymbol{B}}{\partial t} = -c\boldsymbol{\nabla} \times \boldsymbol{E}, \tag{3}$$

using a simple leapfrog algorithm (assuring the satisfaction of $\boldsymbol{\nabla} \cdot \boldsymbol{B} = 0$ with numerical accuracy). The particle positions and momenta are advanced in time in a leapfrog scheme, using the Vay pusher algorithm for advancing the momenta under the local Lorentz force (Vay 2008). Our implementation is nominally of second-order accuracy, although the main source of inaccuracy is the limited number of macroparticles per grid cell.

Our simulations were performed in a cubic domain of physical size L ($-L/2 \leqslant x, y \leqslant L/2$; $0 \leqslant z \leqslant L$). Introducing a cylindrical coordinate system ($0 \leqslant r \leqslant R_{\rm out}$; $0 \leqslant \phi < 2\pi$) centered along the $x = y = 0$ axis, one can fit in this domain an axially and translationally symmetric equilibrium with the outer radius $R_{\rm out} = L/2$. The equilibrium is based on the radial profile of toroidal magnetic field $B_\phi(r)$ in the form of a power law with inner and outer cutoffs (see the upper left panel of Figure 1):

$$B_\phi(r) = B_0 \left(\frac{r}{R_0}\right)^{\alpha_{\rm B\phi}} C(\alpha_{\rm B\phi}, r) C(\alpha_{\rm B\phi}, R_{\rm out} - r), \tag{4}$$

$$C(\alpha_{\rm B\phi}, r) = \frac{(r/R_0)^{1-\alpha_{\rm B\phi}}}{1 + (r/R_0)^{1-\alpha_{\rm B\phi}}},$$

with a *toroidal field index* $\alpha_{\rm B\phi} \leqslant 0$ and a *core radius* $R_0 = R_{\rm out}/10 = L/20$. These profiles peak at radii $R_{\rm peak}/R_0 \simeq 0.84$, 1, 1.55, and 5, for $\alpha_{\rm B\phi} = -1.5$, -1, -0.5, and 0, respectively. In order to achieve the most consistent scaling of our results with $\alpha_{\rm B\phi}$, we introduce a characteristic radius $R_{\rm B\phi}$ that is equal to $R_{\rm peak}$ for $\alpha_{\rm B\phi} = -1.5$, -1, and -0.5, and equal to $R_{\rm peak}/2$ for $\alpha_{\rm B\phi} = 0$.

The initial equilibrium is provided by the axial electric current $j_z(r) = (c/4\pi r) d(rB_\phi)/dr$, as well as by a combination of the axial magnetic field $B_z(r)$ and the radial gas pressure $P_{rr}(r)$:

$$\frac{B_\phi}{4\pi r}\frac{d(rB_\phi)}{dr} + \frac{1}{8\pi}\frac{dB_z^2}{dr} + \frac{dP_{rr}}{dr} = 0. \tag{5}$$

We introduce a constant *pressure mixing parameter* $f_{\rm mix} \in [0: 1]$, which is the fraction of the toroidal magnetic stress that is balanced by the gas pressure (with the remainder balanced by the axial magnetic pressure):

$$\frac{dP_{rr}}{dr} = -f_{\rm mix}\frac{B_\phi}{4\pi r}\frac{d(rB_\phi)}{dr}, \tag{6}$$

$$\frac{dB_z^2}{dr} = -(1 - f_{\rm mix})\frac{2B_\phi}{r}\frac{d(rB_\phi)}{dr}. \tag{7}$$

The case $f_{\rm mix} = 0$ means that B_ϕ is balanced entirely by B_z (with uniform gas pressure; the FF screw-pinch), and the case $f_{\rm mix} = 1$ means that B_ϕ is balanced entirely by the gas pressure ($B_z = 0$; the Z-pinch). For $\alpha_{B\phi} = -1$ and $f_{\rm mix} < 1$ ($B_z \neq 0$), the magnetic pitch profile $\mathcal{P}(r) = rB_z(r)/B_\phi(r)$ is almost constant at $\mathcal{P}_0 = R_0\sqrt{1 - f_{\rm mix}}$ for $r < R_0$, then slightly decreasing with r, and then strongly increasing with r for $r > 4.5\,R_0$. In the FF limit $f_{\rm mix} = 0$, we have $\mathcal{P}_0 = R_0$, and since $L/\mathcal{P}_0 = 20 > 2\pi$, the Kruskal–Shafranov stability criterion is not satisfied, hence this configuration is predicted to be unstable (e.g., Bromberg et al. 2019).

For $f_{\rm mix} < 1$, we also introduce a toroidal component of electric current density:

$$j_\phi(r) = (1 - f_{\rm mix})\frac{c}{4\pi r}\frac{B_\phi}{B_z}\frac{d(rB_\phi)}{dr}. \tag{8}$$

The initial profile of gas pressure $P_{rr}(r)$ determines the initial profile of gas density $n(r) = P_{rr}(r)/\Theta_0 m_{\rm e}c^2$ for a uniform initial relativistic temperature $\Theta_0 = k_{\rm B}T_0/m_{\rm e}c^2$, where $m_{\rm e}$ is the electron mass, $k_{\rm B}$ is the Boltzmann constant, and T_0 is the initial temperature in kelvins. In our simulations, we have adopted an ultrarelativistic temperature with $\Theta_0 = 10^4$. In this work, we neglect the effects of radiative cooling, leaving this important topic for a future study.

In the case of nonuniform gas pressure ($f_{\rm mix} > 0$), the gas density profile is normalized by adding a constant value to obtain the desired *density contrast* $\xi_n \equiv n_{\rm max}/n_{\rm min}$—the ratio of maximum (central) $n_{\rm max}$ to minimum $n_{\rm min}$ density values. Two values have been adopted for the density contrast: a moderate value of $\xi_n = 10$ and a high value of $\xi_n = 100$. The density contrast is particularly important for determining the radial profile of the *hot magnetization* based on the total magnetic field $\sigma_{\rm hot}(r) = B^2(r)/4\pi w(r)$, where $w(r) \simeq 4\Theta_0 n(r) m_{\rm e}c^2$ is the relativistic enthalpy density. A higher density contrast results in a lower gas density and higher magnetization outside the central core region (see Figure 1).

The case $f_{\rm mix} = 0$ requires a uniform gas pressure, and hence a uniform gas density, which corresponds to a density contrast of $\xi_n = 1$. In this case, the gas density is normalized to a value such that the drift velocity profile $\beta_{\rm d}(r) = \boldsymbol{j}(r)/cen(r)$ satisfies the condition that $\max(\beta_{\rm d}) = 0.5$.[10] For all other cases, we make sure that $\beta_{\rm d}(r) \leqslant 0.5$.

The minimum value of gas pressure is given by $P_{\rm min} = \Theta_0 n_{\rm min} m_{\rm e}c^2$. In the cases that involve axial magnetic field ($f_{\rm mix} < 1$), we also add a small constant to $B_z(r)$, such that it satisfies the relation $\min(B_z^2) = 10^{-3}\max(B_z^2)$.

The key parameters of the initial configuration are thus $f_{\rm mix}$, $\alpha_{\rm B\phi}$, and ξ_n. Their values for our main simulations are listed in

[10] Note that the axial current density peaks at $r = 0$ at the level of $j_{\rm max} \simeq cB_0/2\pi R_0$, which implies a lower limit on the particle density $n_{\rm max} \simeq j_{\rm max}/ce\beta_{\rm d} \gtrsim B_0/\pi e R_0$, which in turn implies an upper limit on the magnetization of $\sigma(r) \lesssim (B/B_0)^2 (n/n_{\rm max})^{-1}(R_0/16\rho_0)$, which depends primarily on the scale separation between ρ_0 and R_0.

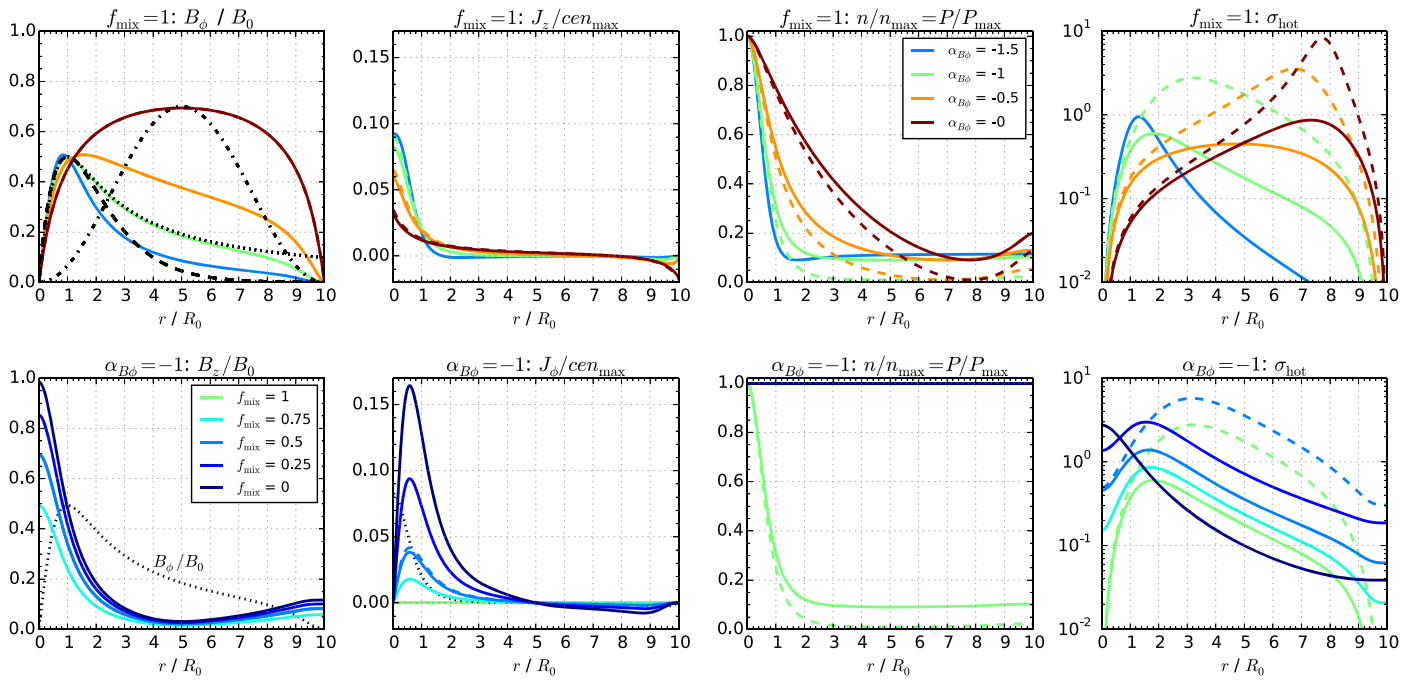

Figure 1. *Upper row of panels*: initial configurations compared for the series of simulations with gas pressure balance ($f_{\rm mix}=1$) and different toroidal field indices $\alpha_{B\phi}$ (indicated by line colors defined in the legend). *From left to right:* radial profiles of the initial toroidal magnetic field $B_\phi(r)$ in units of B_0; radial profiles of the axial current density $j_z(r)$ normalized to $cen_{\rm max}$; radial profiles of the gas density $n(r)$ normalized to $n_{\rm max}$ (proportional to the gas pressure $P(r)/P_{\rm max}$); and radial profiles of the initial hot magnetization $\sigma_{\rm hot}(r)$. For comparison with the configuration of our simulations, in the upper left panel we also show the "constant pitch" profile simulated by Mizuno et al. (2009), Bromberg et al. (2019), and Davelaar et al. (2020) (dotted black line); the exponentially decaying profile of Alves et al. (2018, 2019) (dashed black line); and the "sinusoidal" profile of O'Neill et al. (2012) (dashed–dotted black line). *Lower row of panels:* initial configurations compared for the series of simulations with the same toroidal field index $\alpha_{B\phi}=-1$ and different pressure-mixing parameters $f_{\rm mix}$ (indicated by line colors defined in the legend). *From left to right:* radial profiles of the initial axial magnetic field $B_z(r)/B_0$ (and the common profile of $B_\phi(r)/B_0$ with the black dotted line); radial profiles of the toroidal current density $j_\phi(r)/cen_{\rm max}$ (and the common profile of $j_z(r)/cen_{\rm max}$ with the black dotted line); radial profiles of the gas density $n(r)/n_{\rm max}=P(r)/P_{\rm max}$; and radial profiles of the initial hot magnetization $\sigma_{\rm hot}(r)$ based on the total magnetic field. In both series, the solid color lines correspond to the moderate density ratio of $\xi_n=10$, and the dashed color lines correspond to the high density ratio of $\xi_n=100$.

Table 1
List of Performed Simulations with the Key Parameters of the Initial Configurations

Label	$f_{\rm mix}$	$\alpha_{B\phi}$	ξ_n
f0_α-1_ξ1	0	−1	1
f025_α-1_ξ10	0.25	−1	10
f05_α-1_ξ10	0.5	−1	10
f05_α-1_ξ100	0.5	−1	100
f075_α-1_ξ10	0.75	−1	10
f1_α-15_ξ10	1	−1.5	10
f1_α-1_ξ10 (ref)	1	−1	10
f1_α-1_ξ100	1	−1	100
f1_α-05_ξ10	1	−0.5	10
f1_α-05_ξ100	1	−0.5	100
f1_α0_ξ10	1	0	10
f1_α0_ξ100	1	0	100

Table 1. The initial radial profiles of $B_\phi(r)$, $B_z(r)$, $j_\phi(r)$, $j_z(r)$, $n(r)\propto P(r)$, and $\sigma_{\rm hot}(r)$ are compared in Figure 1.

Our simulations were performed on a numerical grid size of $N=1152$, with a numerical resolution $dx=dy=dz=L/N=\rho_0/1.28$, where $\rho_0=\Theta_0 m_e c^2/eB_0$ is the nominal particle gyroradius, with e being the positron charge and $R_0/\rho_0=45$. The number of particles of both species per grid cell is 16. The actual set of macroparticles in each cell is drawn from Lorentz-boosted Maxwell–Jüttner distributions, the appropriate moments of which are consistent with $n(r)$, $\beta_{\rm d}(r)$, and Θ_0. The simulation time step was set as $dt=0.99{\rm d}\,x/\sqrt{3}\,c$, according to the Courant–Friedrichs–Lewy (CFL) condition. Digital filtering was applied at every time step to the current and charge densities deposited on the Yee grid. Periodic boundary conditions were adopted at all faces of the Cartesian domain. The edge regions that would correspond to $r>R_{\rm out}$ were initialized with $B_\phi=0$, $\boldsymbol{j}=0$ and uniform B_z, n, P.

Our simulations have a typical duration of $\sim 5\ L/c$. In some cases, we interrupt them at an earlier time, once the perturbations produced by the instability reach the x, y domain boundaries. This is formally defined by considering whether the root mean square of the axial electric field component rms(E_z), calculated within an outer cylindrical shell $9<r/R_0<10$ (see Section 4.1), exceeds the level of $2\times 10^{-3}B_0$. Once that happens during an episode of rapid growth, the simulation is interrupted at the end of that episode.

3. Results: Introducing the Reference Case

We begin the presentation of our results by introducing some basic details on the reference case, which we choose to be the simulation f1_α-1_ξ10 with toroidal field index $\alpha_{B\phi}=-1$ balanced entirely by gas pressure ($f_{\rm mix}=1$), which is the case closest to the configurations investigated by Alves et al. (2018).

Figure 2 presents selected snapshots from the reference simulation. We show 2D (x,z) slices along the $y=0$ plane (containing the symmetry axis $r=0$ of the initial configuration) for the out-of-plane magnetic field component B_y (dominated by the toroidal component B_ϕ) and for the axial electric field component E_z, as well as (x,y) slices along the $z=0$ plane for

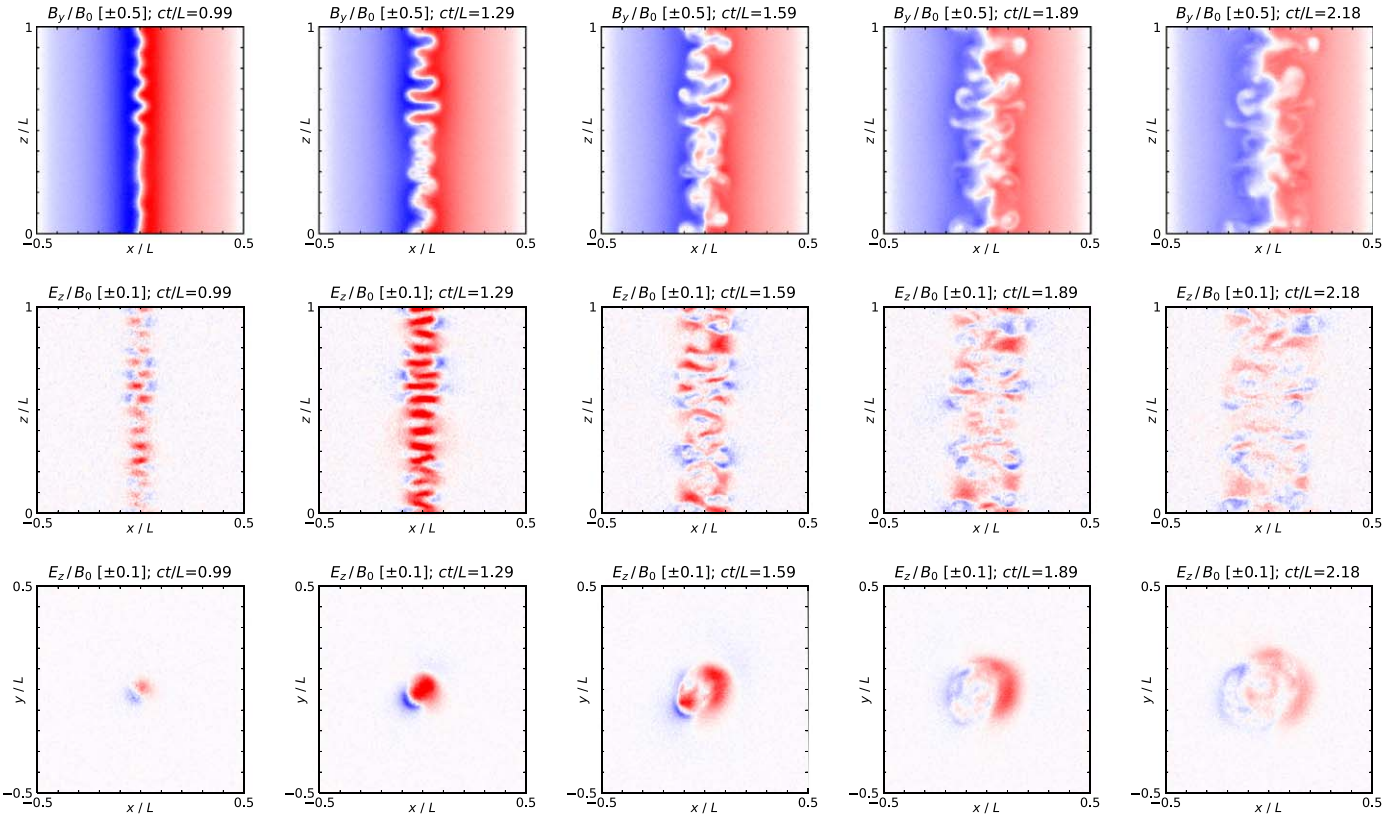

Figure 2. Maps of the magnetic field component B_y (top row of panels) and the electric field component E_z (middle row of panels) in the $y = 0$ plane, as well as the E_z component in the $z = 0$ plane (bottom row of panels), all in units of B_0 (positive values in red, negative in blue), at regular time intervals (from left to right) for the reference simulation f1_α-1_ξ10.

E_z, at five uniformly spaced moments in time. The sequence illustrates the development of unstable modes beginning in the central core region and growing outward. These are characterized by a short wavelength along z ($\lambda_z \simeq 2.7\,R_0$, which means $\simeq$7.5 full wavelengths per L; see Section 4.2) and varying levels of asymmetry in the (x,y) plane, suggesting the dominance of the $m = 1$ kink mode.[11] They break into a nonlinear phase by $t \simeq 1.6\,L/c$. The axial electric field appears to be the strongest and largely positive around $t \simeq 1.3\,L/c$.

The left panels of Figure 3 present the radial profiles of the mean toroidal magnetic field $\langle B_\phi \rangle (r)$ (averaged over z and ϕ) and the mean axial electric field $\langle E_z \rangle (r)$ for the same five moments in time. At $t \simeq L/c$, the toroidal magnetic field profile is still very similar to the initial one, while a net positive axial electric field builds up along the axis. For $1.0 < ct/L < 1.6$, we observe rapid decay of the toroidal magnetic field within $r < 3R_0$. Note from Figure 2 that, by $ct/L \simeq 1.6$, a turbulent structure of both B_y and E_z develops exactly within these radii ($|x| < 0.15L$). Therefore, we consider this decay of B_ϕ as an irreversible magnetic dissipation. We will refer to this period of time as the *fast magnetic dissipation phase*; its beginning and ending are indicated with thick lines. At the end of the fast magnetic dissipation phase ($t \simeq 1.6\,L/c$), $\langle B_\phi \rangle (r)$ peaks at the level of $\simeq 0.28\ B_0$ at a radius of $r \simeq 2.7R_0$. Using these numbers, we can estimate the post-dissipation energy limit as $e(0.28B_0)(2.7R_0) \simeq 0.76\gamma_{\rm lim}$, a rather minor decrease from the initial value. The net axial electric field shoots up to $\simeq 0.07B_0$ in the middle of the fast magnetic dissipation phase and decays to $\simeq 0.02B_0$ by $t \simeq 1.6\,L/c$. For $t > 1.6\,L/c$, dissipation of toroidal magnetic field is significantly slower and $\langle E_z \rangle (r)$ does not exceed $\simeq 0.01\ B_0$.

Figure 4 compares the particle momentum $u = \gamma\beta$ ($u \simeq \gamma$ for $\gamma \gg 1$) distributions dN/du compensated by u^2 for the same five moments in time. The distribution at $t \simeq L/c$ is indistinguishable from the initial Maxwell–Jüttner distribution. The fast magnetic dissipation phase corresponds to a rapid buildup of a high-energy component of the distribution. The high-energy component evolves much more slowly for $t > 1.6\,L/c$. The most energetic particles approach the energy limit, which in our simulations amounts to $\gamma_{\rm lim} = 45\Theta_0$. Based on such momentum distributions, we define the *maximum particle energy* $\gamma_{\rm max}$ as corresponding to the $u_{\rm max}$ value at which $u^2\,dN/du$ equals 10^{-4} of the peak level determined at $t = 0$.

4. Results: Instability Modes

4.1. Pinch versus Kink Modes

Here, we compare the relative strengths of the two fundamental azimuthal instability modes—the $m = 0$ pinch versus the $m = 1$ kink—in both the linear and nonlinear stages. We have analyzed the 3D spatial distributions of the axial electric field component E_z. Using the cylindrical coordinates (r, ϕ, z) centered at the initial symmetry axis, we define a series of cylindrical shells $\mathcal{S}_n$ for $n \in \{1,\ldots,9\}$ delimited by $R_{n-1} < r < R_n$, where $R_n = (n+1)R_0$, so that $R_9 = R_{\rm out}$. For the pinch mode, we have also analyzed the central core region $r < R_0$ (the

[11] A further analysis reveals that this mode is circularly polarized, i.e., the phase ϕ_1 is a strong quasi-periodic function of z and a weak function of simulation time.

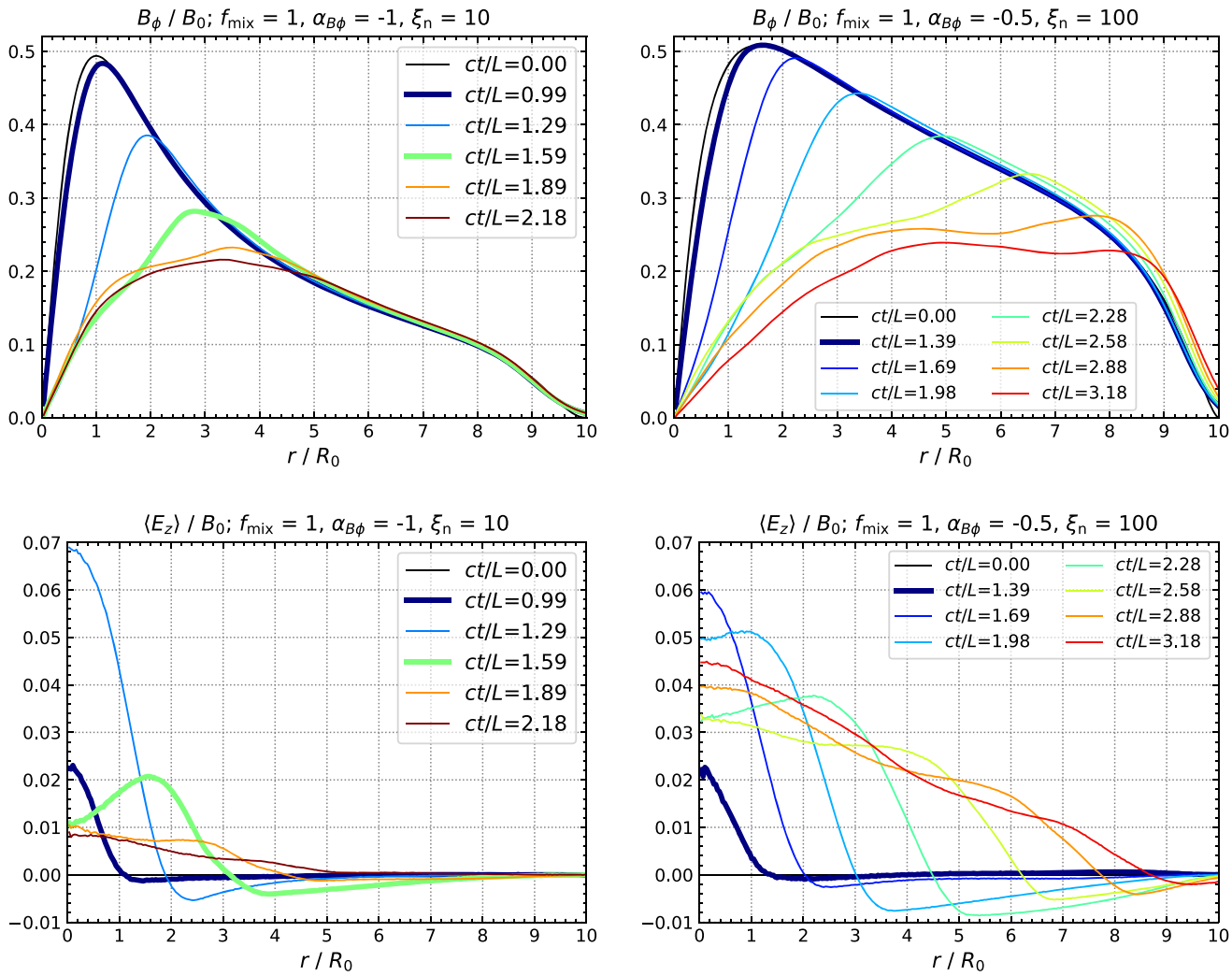

Figure 3. *Top left panel*: radial profiles of the mean toroidal magnetic field $\langle B_\phi \rangle(r)$ (averaged over z and ϕ) for the five moments in time of the reference simulation f1_α-1_ξ10 presented in Figure 2 (and for $t = 0$). *Top right panel*: radial profiles of $\langle B_\phi \rangle(r)$ for the simulation f1_α-05_ξ100. *Bottom panels*: radial profiles of the mean axial electric field $\langle E_z \rangle(r)$ (averaged over z and ϕ) normalized to B_0 for the same moments in time of the same simulations as in the respective top panels.

$\mathcal{S}_0$ shell). Within each shell, the values of E_z have been averaged over r. Then, for every value of z, the function $\langle E_z \rangle(\phi, z)$ has been decomposed into a Fourier series $\sum_m E_m(z)\cos[m\phi + \phi_m(z)]$ with real amplitudes $E_m(z)$ and phases $\phi_m(z)$. These amplitudes have been averaged over z and will be presented as functions of simulation time.

Figure 5 presents the spacetime diagrams (r,t) of the amplitudes of the pinch and kink modes for two simulations, including all nine shells $\{\mathcal{S}_1,\ldots,\mathcal{S}_9\}$, and for the pinch mode also the core region $\mathcal{S}_0$. In the reference case f1_α-1_ξ10 (two left panels in Figure 5), we find a strong pinch mode (with $E_0 \sim 0.1B_0$) highly localized in both radius and time. In the core region, it is found for $1.0 < ct/L < 1.5$, which is during the fast magnetic dissipation phase. It is also found in the first shell $\mathcal{S}_1$ during a slightly later period of $1.3 < ct/L < 1.6$. A slightly weaker kink mode is more extended in both time and radius. In the first shell, it can be seen for $1.1 < ct/L < 1.8$; in the next two shells ($2 < r/R_0 < 4$) it is successively delayed at a rate similar to that for the pinch mode. These modes appear to originate in the central core region and propagate radially outward. At lower amplitude levels of $\sim 10^{-3}B_0$, the pinch mode appears to propagate at a velocity of $\sim 0.4c$, faster than the kink mode ($\sim 0.2c$).

In the case f1_α0_ξ100 (two right panels in Figure 5), both the pinch and the kink modes achieve higher amplitudes of $\sim 0.1B_0$, starting around $t \simeq 2\,L/c$ and lasting at least until $t \simeq 4.3\,L/c$, at which point the simulation has been interrupted because the modes reached the outer boundary according to the criterion described in Section 2. Both modes appear to originate in the central core and propagate outward with similar velocities $\sim 0.2\,c$. Looking at the amplitude levels of $\sim(10^{-2.5}$–$10^{-2.0})B_0$ of the pinch mode, we see an excess signal in the $\mathcal{S}_5$, $\mathcal{S}_6$ shells ($5 < r/R_0 < 7$) at $ct/L \simeq 2.5$–3. Such a signal is not seen in the kink mode, and it also is not found (at least that clearly) in our other simulations. We discuss the origin of this radially localized pinch mode in Section 6.

We now focus on the first shell $\mathcal{S}_1$ ($1 < r/R_0 < 2$). Figure 6 compares the time evolutions of the $m = 0$, 1, and 2 modes for two series of simulations: $f_{\rm mix} = 1$ (varying $\alpha_{B\phi}$ and ξ_n) and $\alpha_{\rm B\phi} = -1$ (varying $f_{\rm mix}$ and ξ_n). In the $f_{\rm mix} = 1$ series (upper panels in Figure 6), the amplitudes of the $m = 0$ pinch modes are comparable to the amplitudes of the $m = 1$ kink modes, and the $m = 2$ modes are only slightly weaker. With the simulation time t scaled by the characteristic radius $R_{\rm B\phi}$, the evolutions of the modes are similar for different values of $\alpha_{\rm B\phi}$. At the same time, the mode evolution is not sensitive

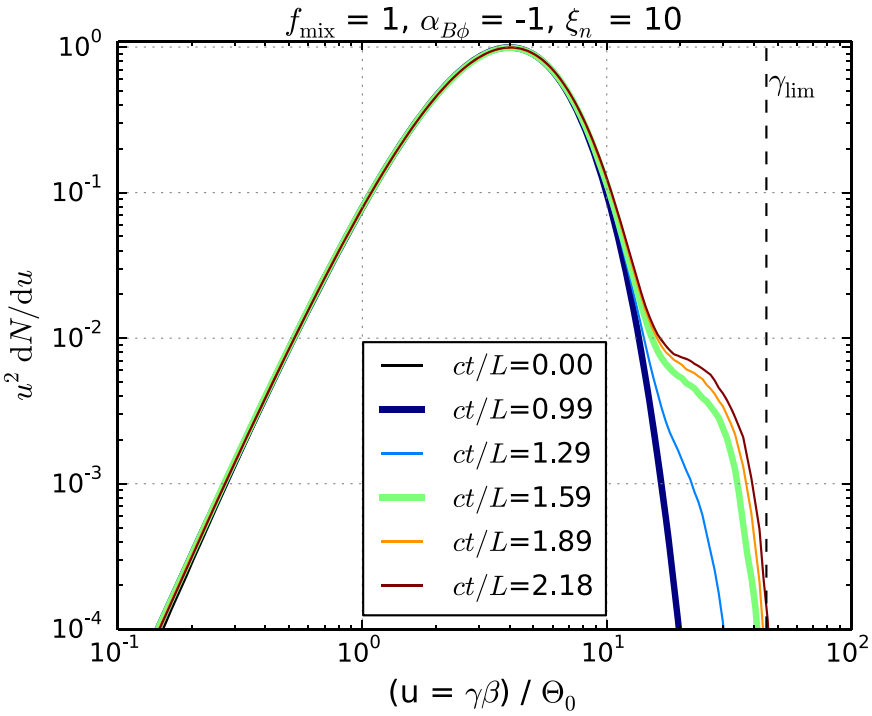

Figure 4. Particle momentum distributions $u^2\ dN/du$ (equivalent to energy distributions since $\Theta_0 \gg 1$), combined for both electrons and positrons and normalized to peak at unity, for the five moments in time of the reference simulation f1_α-1_ξ10 presented in Figure 2. The vertical dashed line indicates the *confinement* energy limit $\gamma_{\rm lim} = 45\Theta_0$.

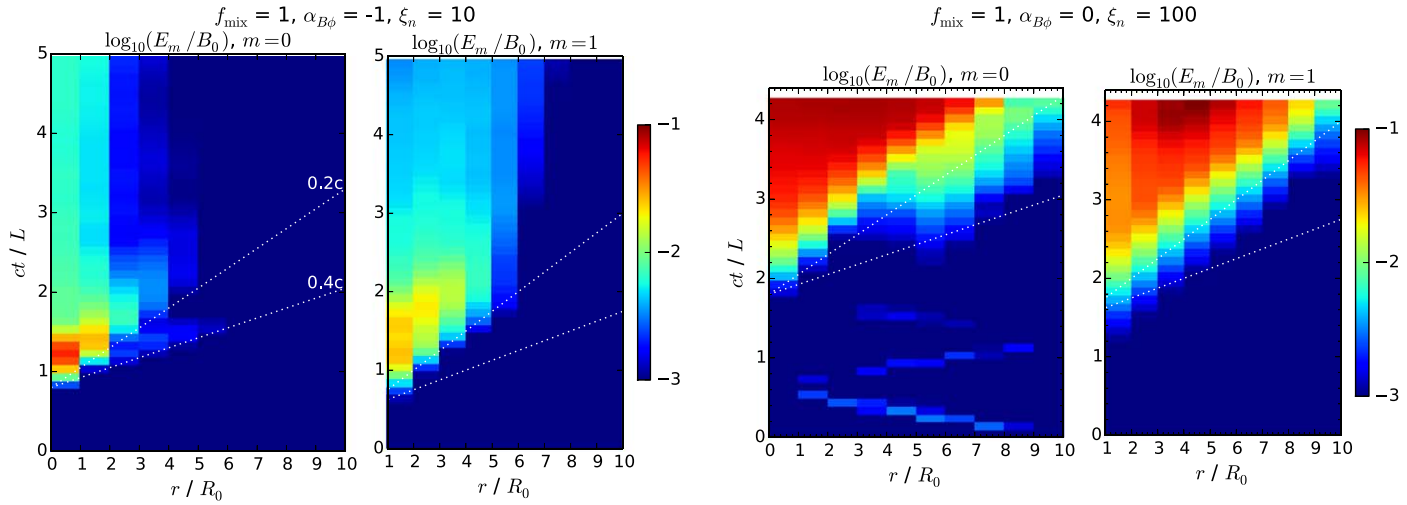

Figure 5. Spacetime diagrams of the amplitudes E_m (averaged over z) of the azimuthal modes m of the $E_z(\phi, z)$ distributions compared for two simulations. The white dotted lines indicate the speed levels of $0.2c$ and $0.4c$. In the case f1_α0_ξ100, the simulation was interrupted at $ct/L \simeq 4.27$ when the perturbations reached the boundary according to the definition described in Section 2.

to the density contrast ξ_n, especially in the linear stage. In all simulations, we find that the kink mode is the first to emerge (roughly when $\langle E_1 \rangle$ exceeds the $10^{-3}B_0$ level) followed by the pinch mode and all the higher modes ($m \geqslant 2$).

In the $\alpha_{B\phi} = -1$ series (lower panels in Figure 6), we observe a systematic weakening of the pinch mode together with a strengthening of the kink mode with decreasing value of $f_{\rm mix}$ (in agreement with the linear analysis of Bodo et al. 2013). The reason for this is that the axial magnetic flux resists radial compression, and hence stabilizes the $m = 0$ pinch mode for $f_{\rm mix} \to 0$. For $f_{\rm mix} < 1$, the evolution of the pinch mode does not even show regular linear stages of exponential growth, while the kink mode shows linear stages extending over two orders of magnitude in $\langle E_1 \rangle$, reaching values up to $0.1B_0$ in the case $f_{\rm mix} = 0.5$ and $\xi_n = 100$. Higher modes ($m \geqslant 2$) are once again systematically weaker and delayed.

We have measured the minimum growth timescales $\tau_{\rm min} = (c\Delta t/R_{B\phi})\min(1/\Delta \ln \langle E_m \rangle)$ for each mode m in every studied case; their values are compared in Figure 7 (the corresponding segments of the $\langle E_m \rangle(t)$ functions are indicated in Figure 6). One should note that the time resolution for this analysis is limited to $\Delta t \simeq 2R_0/c$, hence any shorter timescales should be considered as upper limits. Nevertheless, our results indicate that the pinch modes are typically the fastest ones ($\tau_{\rm min} < 2$ for $f_{\rm mix} = 1$), and the kink modes are typically the slowest ones ($\tau_{\rm min} > 2$). In general, the value of $\tau_{\rm min}$ decreases with

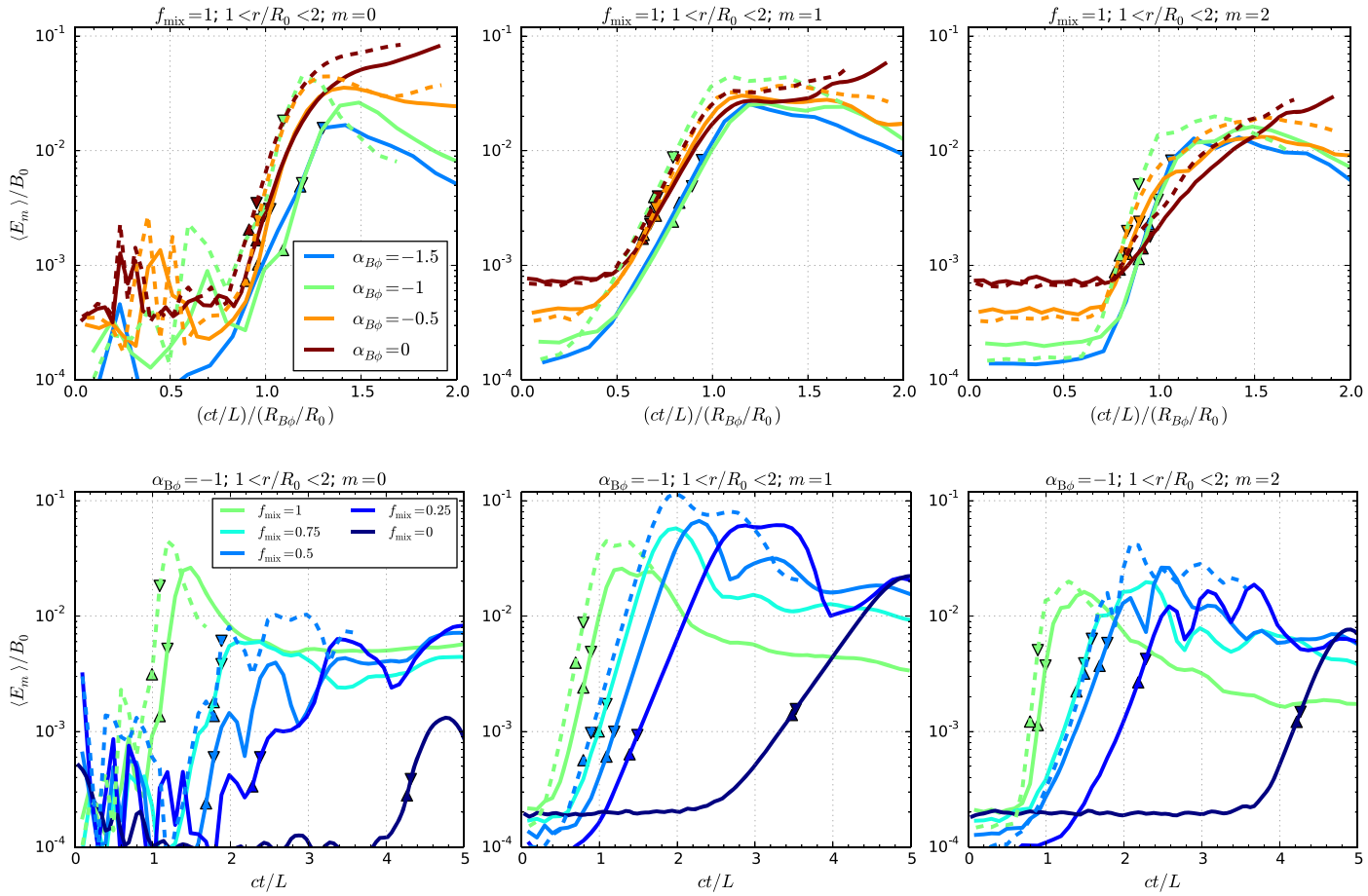

Figure 6. Amplitudes E_m of the azimuthal modes m of the axial electric field E_z extracted from the $1 < r/R_0 < 2$ cylindrical shell, averaged over z and presented as functions of the simulation time t scaled by the characteristic radius $R_{\rm B\phi}$. The upper row of panels compares the simulations with $f_{\rm mix} = 1$, different values of $\alpha_{\rm B\phi}$ (indicated by the line color), and different values of ξ_n (10: solid lines, 100: dashed lines). The lower row of panels compares the simulations with $\alpha_{\rm B\phi} = -1$, different values of $f_{\rm mix}$ (indicated by the line color), and different values of ξ_n (as before). The left panels show the $m = 0$ pinch mode, the middle panels show the $m = 1$ kink mode, and the right panels show the $m = 2$ mode. The triangles indicate the line segments for which the growth timescale τ of the mode amplitude is minimized.

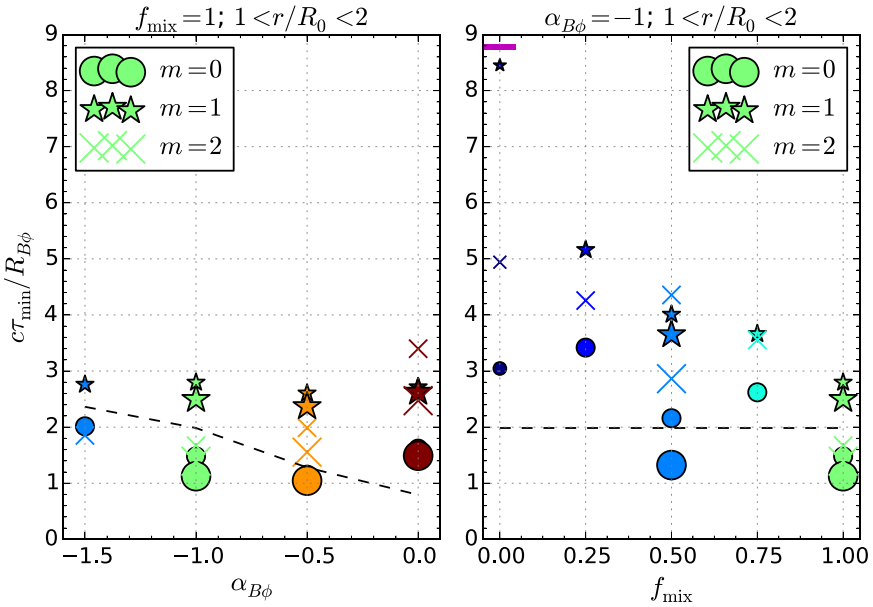

Figure 7. Minimum growth timescales $\tau_{\rm min}$ normalized to $R_{\rm B\phi}/c$ evaluated for the amplitudes E_m of the azimuthal modes of E_z presented in Figure 6. The symbol colors correspond to the line colors used in Figure 6. Different symbol types indicate the mode number m. For each symbol type, the smaller symbols correspond to $\xi_n = 10$, and the larger symbols correspond to $\xi_n = 100$ (except for the case $f_{\rm mix} = 0$, in which $\xi_n = 1$). The short magenta line in the right panel indicates the analytical prediction for the $|m| = 1$ kink mode in the constant-pitch FF configuration (Appl et al. 2000). The black dashed lines mark the time-resolution limit for this analysis.

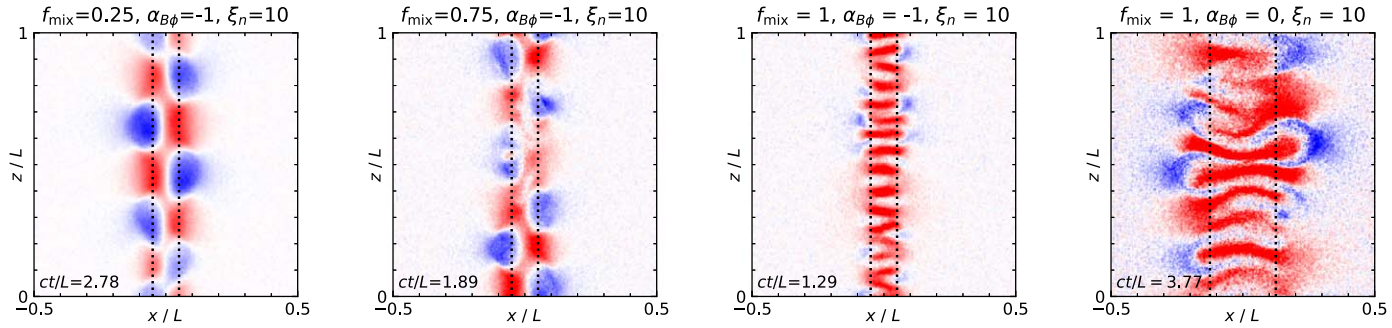

Figure 8. Maps of electric field component E_z in units of B_0 (positive values in red, negative in blue) in the $y = 0$ plane, compared for several simulations at the moments (indicated in the bottom left corners) of peak root-mean-square value of E_z evaluated at $r = R_0$. The vertical dotted lines indicate $r = R_{B\phi}$, which equals R_0 for $\alpha_{B\phi} = -1$ and $2.5R_0$ for $\alpha_{B\phi} = 0$.

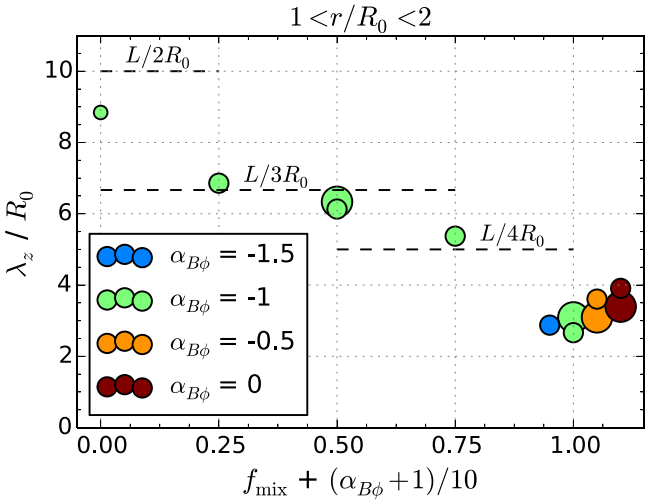

Figure 9. Effective axial wavelength λ_z of the $\langle E_z \rangle(z)$ fluctuations measured within the cylindrical shell region $\mathcal{S}_1$ ($1 < r/R_0 < 2$) at the moments of peak rms(E_z). The smaller symbols correspond to $\xi_n = 10$, and the larger symbols correspond to $\xi_n = 100$ (except for the case $f_{mix} = 0$, in which $\xi_n = 1$).

increasing f_{mix}, and its dependence on $\alpha_{B\phi}$ is captured by its explicit scaling with $R_{B\phi}$.

4.2. Effective Axial Wavelength

Figure 8 compares the (x,z) maps in the $y = 0$ plane of the axial electric field component E_z for four selected simulations at the moments when the root-mean-square values of E_z evaluated at the central core radius $r = R_0$ achieve their peaks. In the case f025_α-1_ξ10, we observe a regular structure with the regions of $E_z > 0$ (red) slightly more extended than the regions of $E_z < 0$ (blue), aligned asymmetrically about the central axis (indicating the dominance of the kink mode), with three full wavelengths over $\Delta z = L$. In the case f075_α-1_ξ10, the structure of $E_z(x, z)$ appears to be very similar to the previous case; however, some short-wavelength kink-like fluctuations appear superposed. In the reference case f1_α-1_ξ10 (see Figure 2), we find a very different structure of E_z, in the form of a somewhat irregular stack of $\simeq$16 short-wavelength patches of positive values, separated by narrow gaps of weak (but still positive) values. This can be compared with the last presented case f1_α0_ξ10, in which the $E_z > 0$ patches are much more extended radially, because in this case the evolution of the instability is longer by a factor $\simeq R_{B\phi}/R_0 = 2.5$.

Using the (r)-averaged profiles of $\langle E_z \rangle(\phi, z)$ extracted from the first cylindrical shell region $\mathcal{S}_1$, we calculated the discrete Fourier transform $E_k(\phi) = \sum_j \langle E_z \rangle(\phi, z_j) \exp(-2\pi i k z_j/L)$ over a regular grid $0 \leqslant z_j < L$, averaged the $E_k(\phi)$ amplitudes over ϕ, then calculated the effective axial wavenumber $\langle k_z \rangle = (\sum_k k E_k^2)/(\sum_k E_k^2)$, and finally obtained the corresponding effective wavelength $\lambda_z = 2\pi/\langle k_z \rangle$. Figure 9 compares the values of λ_z for all our simulations. We find that λ_z is decreasing systematically with increasing f_{mix}. For $f_{mix} = 0$, we find that $\lambda_z \simeq 8.8R_0 \simeq L/2.25$, which reflects the dominance of two full wavelengths in the E_z structure. For $f_{mix} \sim 0.25$–0.5, λ_z is consistent with $L/3$. For $f_{mix} = 0.75$, the effective wavelength is $\lambda_z \simeq 5.4R_0 \simeq L/3.7$, in agreement with a combination of long $(L/3)$ current-driven modes characteristic of the FF screw-pinches and short pressure-driven modes characteristic of the Z-pinches (see the second left panel of Figure 8). For $f_{mix} = 1$, all of our simulations produce consistent values of $\lambda_z \simeq (2.7$–$3.9)R_0 \simeq (L/7.5$–$L/5)$, increasing somewhat with increasing $\alpha_{B\phi}$, but not scaling clearly with $R_{B\phi}$. There is little dependence of λ_z on the density ratio parameter ξ_n.

5. Results: Particle Acceleration

5.1. Fast Magnetic Dissipation Phase and Particle Energy Limit

In this subsection, we show that the Z-pinch configurations with steep toroidal field indices ($\alpha_{B\phi} \leqslant -1$) satisfy the γ_{lim} energy limit, while those with shallow indices ($\alpha_{B\phi} > -1$) exceed that limit. Energetic particles are well-confined within the jet core in either case. For $\alpha_{B\phi} \leqslant -1$, efficient magnetic dissipation proceeds over a limited period of time, transitioning from a *fast magnetic dissipation phase* to a slow magnetic dissipation phase before the perturbations reach the domain boundaries. We will argue that particle energies are limited by the finite time duration of the fast magnetic dissipation phase.

5.1.1. The Reference Case $f_{mix} = 1$ and $\alpha_{B\phi} = -1$

Figure 10 compares in detail the time evolutions of the toroidal magnetic flux (calculated as $\Psi_{B\phi} \propto \langle |B_y| \rangle$ with averaging over x and z along the $y = 0$ plane), the total magnetic energy $\mathcal{E}_B$, the mean axial electric field at $r = R_0$, and the maximum particle energy as a fraction of the energy limit, $\gamma_{max}/\gamma_{lim}$. The first thing to notice is that the relative decrease of toroidal magnetic flux (the thick green line) is very similar to the relative decrease of total magnetic energy (the thin green line), the main difference being an earlier onset

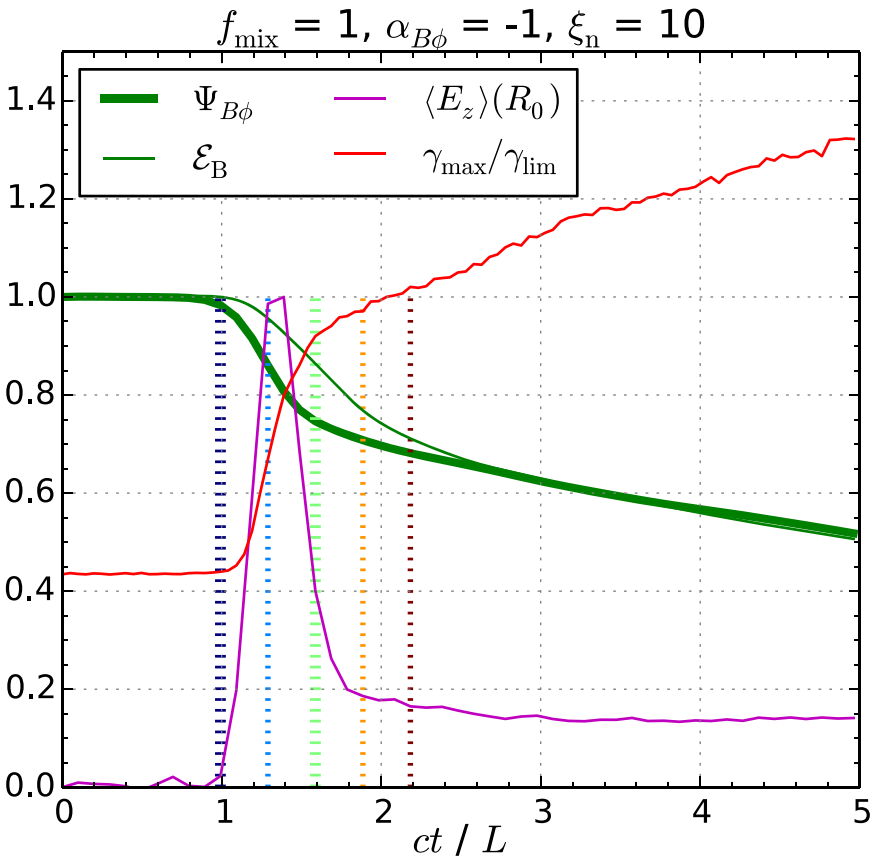

Figure 10. Time evolutions of the toroidal magnetic field B_ϕ and axial electric field E_z for the reference simulation f1_α-1_ξ10. The thick green line shows the toroidal magnetic flux $\Psi_{B\phi}$ normalized to its initial value; the thin green line shows the total magnetic energy $\mathcal{E}_{\rm B}$ normalized to its initial value; the red line shows the maximum particle energy $\gamma_{\rm max}$ normalized to the Lorentz factor limit $\gamma_{\rm lim}$; the magenta line shows the mean axial electric field $\langle E_z\rangle$ (averaged over z and ϕ) evaluated at $r = R_0$ and normalized to its peak value of $E_{z,\rm peak} = 0.043B_0$; the five vertical thick dotted lines indicate the five moments in time presented in Figure 2–4.

of the toroidal flux dissipation. The toroidal magnetic flux clearly shows two phases of magnetic dissipation—a fast magnetic dissipation phase for $1.0 < ct/L < 1.6$, followed by a slow magnetic dissipation phase (this is consistent with the results of Bodo et al. 2022).

Let us now discuss the evolution of the mean axial electric field $\langle E_z\rangle(R_0)$. The fast magnetic dissipation phase involves a temporary spike of $\langle E_z\rangle(R_0)$, peaking at the level of $\langle E_z\rangle_{\rm peak} \simeq 0.043B_0$ for $t \sim (1.3\text{–}1.4)\,L/c$, simultaneous with the most rapid increase of $\gamma_{\rm max}$.[12] To illustrate the connection between the electric field strength at $r = R_0$ and evolution of $\gamma_{\rm max}$, consider a slightly different time period of $1.2 < ct/L < 1.7$, during which $\langle E_z\rangle(R_0)$ exceeds the level of $0.2\langle E_z\rangle_{\rm peak}$. During that time period of $\Delta t \simeq 0.5\,L/c$, $\gamma_{\rm max}$ increases by $\Delta\gamma_{\rm max} \simeq 18.8\Theta_0 \simeq 0.42\gamma_{\rm lim}$.This energy gain corresponds to linear acceleration by the average electric field of $\langle E_{\rm acc}\rangle/B_0 = (L/\rho_0)^{-1}\,\Delta(\gamma_{\rm max}/\Theta_0)/\Delta(ct/L) \simeq 0.042 \simeq \langle E_z\rangle_{\rm peak}/B_0$. Hence, the electric field strength $\langle E_{\rm acc}\rangle$ required to explain the acceleration of the most energetic particles during that period is consistent with $\langle E_z\rangle_{\rm peak}$.[13] Our analysis of individually tracked particles confirms that the most energetic ones are indeed accelerated within the core region ($r < R_0$), predominantly by the positive axial electric field during the fast magnetic dissipation phase, as stated by Alves et al. (2018).

The typical energy gain of an energetic particle can be derived directly from the duration Δt of the fast magnetic dissipation phase:

$$\frac{\Delta\gamma}{\gamma_{\rm lim}} = \frac{1}{2}\left(\frac{L}{20R_0}\right)\left(\frac{c\Delta t}{L/2}\right)\frac{\langle E_{\rm acc}\rangle}{B_0/20}, \tag{9}$$

where $\langle E_{\rm acc}\rangle$ is the average electric field component along the particle velocity vector. This means that a relatively short duration $\Delta t \sim L/2c$, in combination with realistic electric field strengths, is sufficient to explain one half of the "confinement" limit (also known as the Hillas limit) on the particle energy gain.

As a representative example, let us consider the acceleration history of an individual energetic particle. The left panels of Figure 11 show the history of an energetic positron (denoted as "pos #107") from the reference simulation. This positron is energized from $\simeq 0.2\gamma_{\rm lim}$ to $\simeq 0.6\gamma_{\rm lim}$ during the fast magnetic dissipation phase. The energy gain of $\Delta\gamma \simeq 0.4\gamma_{\rm lim}$ over the timescale of $\Delta t \simeq 0.6\,L/c$ requires an average electric field of $\langle E_{\rm acc}\rangle \simeq B_0/30$, which is consistent with the axial electric field E_z experienced by the positron. In the top panels of Figure 11, the dashed blue line shows that the acceleration of this particle can be attributed almost exclusively to the action of the axial electric field component E_z. Likewise, it can be demonstrated that the action of the electric field component

[12] The fastest e-folding growth timescale of $\langle E_z\rangle(R_0)$ has been estimated as $\tau_{Ez} \simeq 0.046L/c \simeq 0.9R_0/c$ over the period of $1.0 < ct/L < 1.1$. Hence, the duration of the fast magnetic dissipation phase corresponds to $\simeq 13\tau_{Ez}$.

[13] One can note that, on one hand, the average axial electric field at R_0 during that time period should be roughly $\simeq 0.6\langle E_z\rangle_{\rm peak}$; on the other hand, the axial field is somewhat stronger for $r < R_0$.

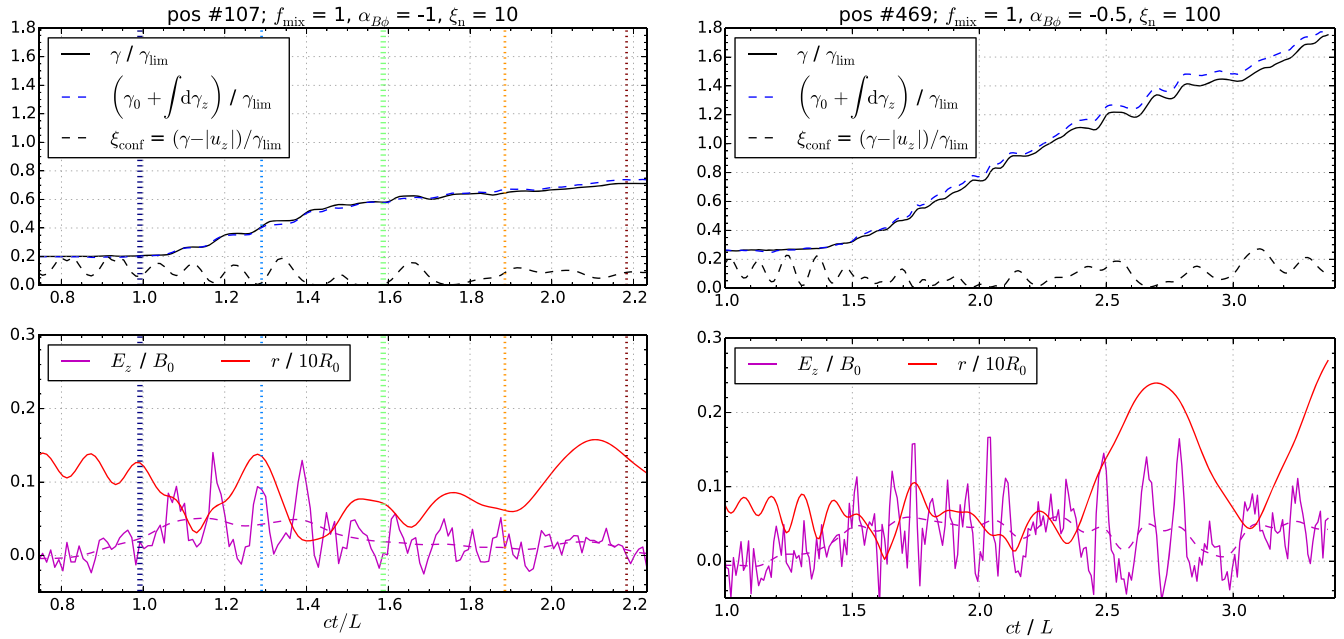

Figure 11. Acceleration histories of single energetic tracked positrons in the reference simulation f1_α-1_ξ10 (left panels) and in the simulation f1_α-05_ξ100 (right panels). In the top panels, the solid black lines show the particle Lorentz factor γ normalized to the energy limit $\gamma_{lim} = eB_0R_0/(mc^2)$; the dashed black lines show the particle confinement indicator $\xi_{conf} = (\gamma - |u_z|)/\gamma_{lim}$ (Appendix A); and the dashed blue lines show what would be the particle Lorentz factor due to the work done by the axial electric field component E_z. In the bottom panels, the solid magenta lines show the local axial electric field component E_z (the dashed magenta lines show its moving average) and the solid red lines show the particle radial coordinate r in units of $10R_0$. The five vertical thick dotted lines in the left panels indicate the five moments in time presented in Figures 2–4.

parallel to the local magnetic field is negligible in this case. During most of the fast magnetic dissipation phase and until $t \simeq 2\,L/c$, this positron is located within the central core at $r < R_0$. In order to determine whether this positron is confined to the central core by toroidal magnetic field, we calculate the *particle confinement indicator* defined as $\xi_{conf} = (\gamma - |u_z|)/\gamma_{lim}$ (see Appendix A). In the present case, we find that $\xi_{conf} < 0.2$ (other energetic particles in this simulation reached $\xi_{conf} \simeq 0.3$), which means that this particle is indeed confined (as are the others). The acceleration rate slows down significantly around the end of the fast magnetic dissipation phase at $t \simeq 1.6\,L/c$. The sole reason for slower acceleration is that the electric fields within the central core become weaker.

We have thus demonstrated in our reference case that the evolution of the toroidal magnetic field includes the fast magnetic dissipation phase, the short duration of which can explain a significant part of the particle energy limit γ_{lim}.

5.1.2. The Effects of $\alpha_{B\phi} > -1$ and $f_{mix} < 1$

In our other simulations, we have explored the effects of three parameters: the pressure mixing ratio f_{mix}, the toroidal field index $\alpha_{B\phi}$, and the density contrast ξ_n. Figure 12 presents the time evolutions of the maximum particle energy γ_{max}: the left panel compares all $f_{mix} = 1$ cases (for different $\alpha_{B\phi}$ and ξ_n) and the right panel compares all $\alpha_{B\phi} = -1$ cases (for different f_{mix} and ξ_n). The reference simulation f1_α-1_ξ10 is displayed as the solid green line in each panel. The values of γ_{max}, as well as the simulation time t, have been scaled by the characteristic radius $R_{B\phi}$, which depends on $\alpha_{B\phi}$ (see Section 2). One can see that γ_{max} begins to increase significantly from its initial value after at least $ct/L \gtrsim R_{B\phi}/R_0$. For $f_{mix} = 1$, it typically shows a single phase of rapid growth to the energy limit γ_{lim} at rates corresponding to acceleration by electric fields $E_{acc} \sim (0.05\text{–}0.08)B_0$. In cases where γ_{lim} is exceeded, the further increase of γ_{max} slows down significantly ($E_{acc} < 0.01B_0$ for $\alpha_{B\phi} = -1.5$, -1 and $\xi_n = 10$). The evolution of γ_{max} is more complex in the $f_{mix} < 1$ cases; in some of them, the γ_{lim} limit is reached in two stages, with E_{acc} only up to $\sim 0.02B_0$. The results for a high density contrast value of $\xi_n = 100$ suggest that the value of γ_{lim} is also relevant to those cases. Among the $\alpha_{B\phi} > -1$ cases, the rescaled $\gamma_{max}/(R_{B\phi}/R_0)$ reaches the γ_{lim} limit for $\alpha_{B\phi} = -0.5$, as well as for $\alpha_{B\phi} = 0$ and $\xi_n = 100$, although we cannot say whether it would flatten subsequently if these simulations could be continued. Particle acceleration appears to be faster for higher values of f_{mix}; this is consistent with the correspondingly shorter instability growth timescales τ_{min}, as shown in Figure 7.

Figure 13 compares the particle momentum distributions between the simulations for $\alpha_{B\phi} = -1$ (hence $R_{B\phi} = R_0$), $\xi_n = 10$ (with one exception of $\xi_n = 100$), and different values of the pressure mixing parameter f_{mix}. This comparison is presented at two simulation times, because these simulations evolve at different rates. At $ct/L \simeq 2.5$, when some $f_{mix} = 1$ simulations are already in the slow acceleration phase while the $f_{mix} = 0.25$ case is just at the onset of fast acceleration, the high-energy distribution tails appear fairly regular (γ_{max} increases with increasing f_{mix}), even if they are very weak for $f_{mix} \leqslant 0.5$. At $ct/L \simeq 5$, when most simulations are in their final stages, the high-energy tails are clearly present for $f_{mix} \geqslant 0.25$ (in the case $f_{mix} = 0$, particle acceleration begins only after $ct/L = 5$), although they are rather irregular, with bumps instead of power laws. At $ct/L \simeq 5$, the fractions of particles contained in these high-energy tails are roughly $\simeq$1% and they carry $\simeq$2% of the total particle energy. The case of high density contrast $\xi_n = 100$ for $f_{mix} = 0.5$ at $ct/L \simeq 2.5$ shows significantly higher fractions: $\simeq$5% of particles carrying $\simeq$14% of particle energy.

Figure 14 compares the time evolutions of the toroidal magnetic flux $\Psi_{B\phi}$ (normalized to its initial value) for all

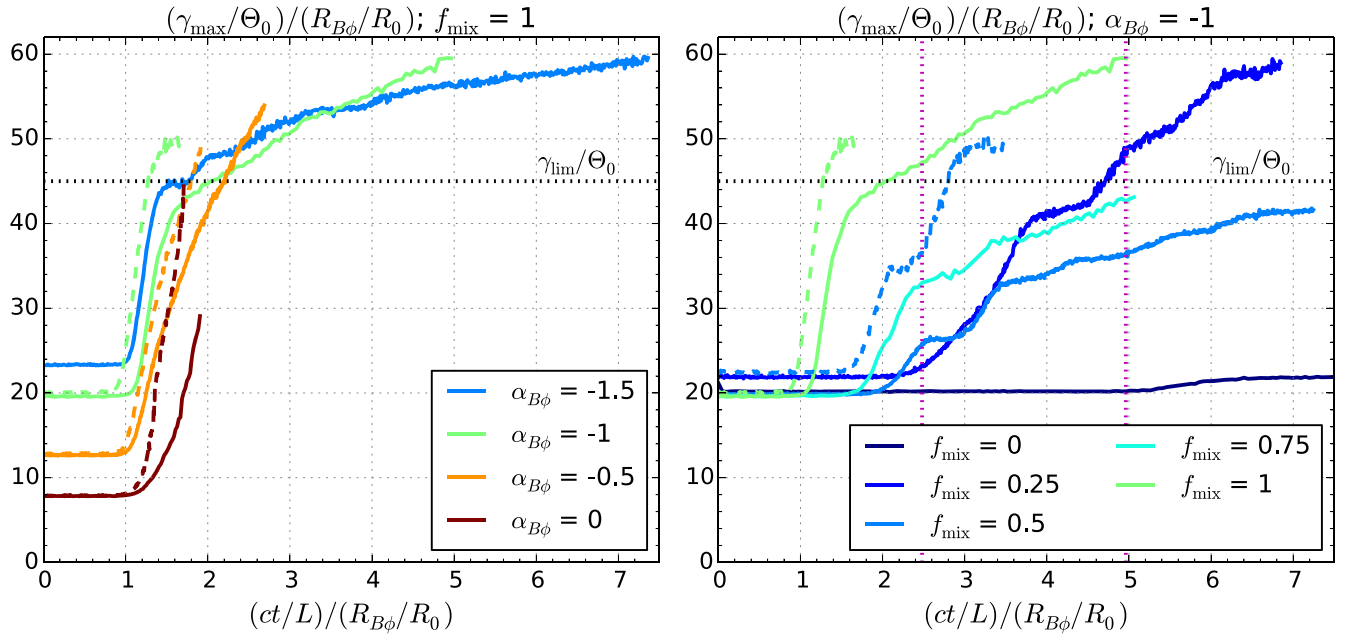

Figure 12. Time evolutions of the maximum particle energy γ_{max} evaluated at the level of 10^{-4} of the $u^2\ dN/du$ particle distributions normalized to peak at unity at $t = 0$. The results are compared for two series of simulations: the left panel shows simulations for $f_{mix} = 1$ and different values of $\alpha_{B\phi}$, and the right panel shows simulations for $\alpha_{B\phi} = -1$ and different values of f_{mix}. Both γ_{max} and the simulation time t are scaled by the characteristic radius $R_{B\phi}$, which depends on $\alpha_{B\phi}$. The solid lines indicate the cases of $\xi_n = 10$, and the dashed lines indicate the cases of $\xi_n = 100$. The horizontal dotted black lines indicate the *confinement* energy limit $\gamma_{lim}/\Theta_0 \equiv R_0/\rho_0 = 45$. The vertical dotted magenta lines in the right panel indicate the times at which particle distributions are compared in Figure 13. The simulations are interrupted at different times, before the perturbations reach the x, y boundaries.

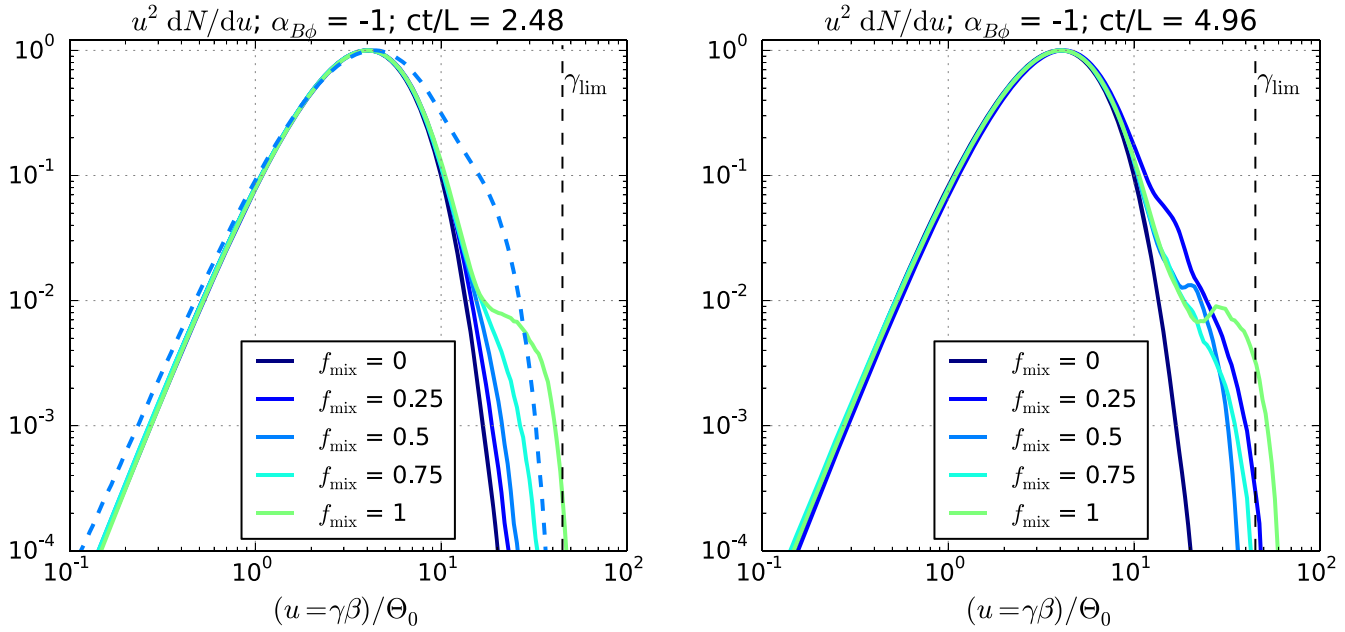

Figure 13. Particle momentum distributions $u^2\ dN/du$ (combined for both electrons and positrons and normalized to peak at unity) compared at two moments in time (left/right panel) between simulations for $\alpha_{B\phi} = -1$, and different values of f_{mix}. The solid lines indicate the cases of $\xi_n = 10$, and the dashed lines indicate the cases of $\xi_n = 100$. The vertical black dashed lines indicate the *confinement* energy limit $\gamma_{lim} = 45\Theta_0$.

simulations. In all cases, we observe an initial period of almost constant $\Psi_{B\phi}$ followed by the onset of the fast magnetic dissipation phase, which in some cases is followed by a transition to a slow magnetic dissipation phase. The simulation time has been scaled by $R_{B\phi}$, such that for $f_{mix} = 1$ the fast magnetic dissipation phases begin roughly at $t \simeq (L/R_0)R_{B\phi}/c \simeq 20R_{B\phi}/c$. On the other hand, for $\alpha_{B\phi} = -1$, these onsets are delayed for the B_z-balanced cases of $f_{mix} < 1$. The overall relative decrease of $\Psi_{B\phi}$ is in the range of ∼(30–60)%. Transitions from the fast magnetic dissipation phase to the slow magnetic dissipation phase can be seen in most cases of $\alpha_{B\phi} \leqslant -1$ (although in some B_z-balanced cases the histories of $\Psi_{B\phi}(t)$ are more complicated). Such a transition is not seen in the cases of $\alpha_{B\phi} > -1$ (although there is a hint of that in the case f1_α-05_ξ10). Comparing Figure 14 with Figure 12, a connection between the evolutions of γ_{max} and $\Psi_{B\phi}$ can be noticed. Simulations in which $\gamma_{max} \gg \gamma_{lim}$ are the same in which the fast magnetic dissipation phase is not

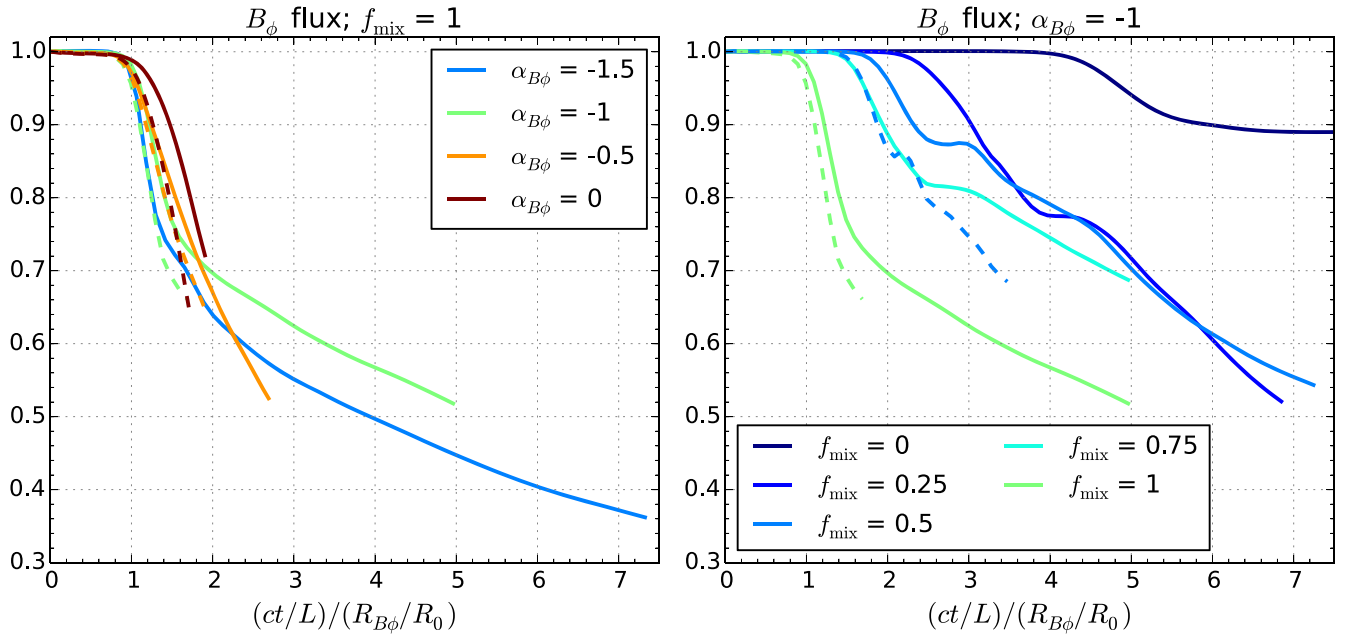

Figure 14. Time evolutions of the toroidal magnetic field flux $\Psi_{B\phi}$, normalized to unity at $t = 0$, compared for two series of simulations, using simulation time t scaled by the characteristic radius $R_{B\phi}$. The line types are the same as in Figure 12.

complete before the perturbations reach the boundaries and the simulation is interrupted. The episodes of rapid increase of $\gamma_{\rm max}$ are simultaneous with a rapid decrease of $\Psi_{B\phi}$.

As an example, let us consider in more detail the case $f_{\rm mix} = 1$, $\alpha_{B\phi} = -0.5$, and $\xi_n = 100$ ($R_{B\phi} = 1.55R_0$; the dashed orange lines in the left panels of Figures 12 and 14). In this case, the fast magnetic dissipation phase begins at $t \simeq 1.4\,L/c$ and lasts until the end of the simulation at $t \simeq 3.4\,L/c$. During that time, $\gamma_{\rm max}$ increases linearly, reaching the level of $\gamma \simeq 90\Theta_0 = 2\gamma_{\rm lim}$. The right panels of Figure 3 show the time evolutions of the radial profiles of $\langle B_\phi\rangle(r)$ and $\langle E_z\rangle(r)$, extending until the simulation ends. The time separations between successive lines are $\Delta t \simeq 0.3\,L/c$, the same as for the reference simulation. Compared with the reference simulation, efficient dissipation of toroidal magnetic field progresses toward larger radii, essentially until it reaches the outer cutoff region. This corresponds to much more extended radial profiles of the net mean axial electric field $\langle E_z\rangle > 0$. The key difference from the reference case is that the axial electric field does not decay in the central core, settling at the value of $\langle E_z\rangle \sim 0.04B_0$ for $r < R_0$, which is four times higher than in the reference case. This is also reflected in the fact that dissipation of toroidal magnetic field in the central core proceeds to deeper levels. The e-folding growth timescale of $\langle E_z\rangle(R_0)$ has been estimated as $\tau_{Ez} \simeq 0.11L/c \simeq 2.2R_0/c$ over the period of $1.1 < ct/L < 1.7$, about 2.4 times longer than in the reference case. This means that, in this simulation, the fast magnetic dissipation phase lasts for at least $\simeq 18\tau_{Ez}$, which is longer in relation to τ_{Ez} than in the reference case.

Having a radially decreasing net axial electric field is key for efficient dissipation of the average toroidal magnetic field, which is governed by the Maxwell–Faraday equation:

$$\frac{\partial\langle B_\phi\rangle}{c\,\partial t} = \frac{\partial\langle E_z\rangle}{\partial r} < 0. \tag{10}$$

For example, the steepest radial gradients of the net axial electric field in both presented cases are $\Delta\langle E_z\rangle \simeq -0.04B_0$ over $\Delta r = R_0$, which corresponds to the peak magnetic dissipation rate of $\Delta\langle B_\phi\rangle/B_0 \simeq -0.8c\Delta t/L$. On the other hand, in the final state of the simulation f1_α-05_ξ100, we have $\Delta\langle E_z\rangle \simeq -0.045B_0$ over $\Delta r = 9R_0$, which yields $\Delta\langle B_\phi\rangle/B_0 \simeq -0.1c\Delta t/L$. These dissipation rates are consistent with the results presented in the top panels of Figure 3.

The right panels of Figure 11 show the acceleration history of an energetic positron (denoted as "pos #469") in the simulation f1_α-05_ξ100. This particle accelerates almost linearly from $\gamma \simeq 0.3\gamma_{\rm lim}$ at $t = 1.4\,L/c$ to $\gamma \simeq 1.75\gamma_{\rm lim}$ at $t = 3.4\,L/c$, which means an energy gain of $\Delta\gamma \simeq 1.45\gamma_{\rm lim}$ over the period of $\Delta t = 2\,L/c$. This acceleration is dominated by action of the axial electric field, which is sustained at the level of $E_z \simeq 0.04B_0$ throughout this time range. For most of the acceleration period (until $t \simeq 2.4\,L/c$), the particle is located within the central core ($r < R_0$), and its confinement indicator is $\xi_{\rm conf} < 0.2$ even as it starts oscillating outside the core at later times. This particle is well-confined by the toroidal magnetic fields, and yet it is able to accelerate beyond $\gamma_{\rm lim}$. Other energetic particles in this simulation reach $\xi_{\rm conf} \simeq 0.6$, and yet they do not escape their confinement and keep accelerating.

5.2. Parallel versus Perpendicular Acceleration

We have addressed the problem of comparing the relative importance of parallel and perpendicular electric fields in particle acceleration by analyzing large samples of individually tracked particles, denoted with index i, for which we recorded as functions of simulation time their energy histories $\gamma_i(t)$, as well as the local magnetic and electric field vectors $\boldsymbol{B}_i(t)$, $\boldsymbol{E}_i(t)$. Out of these samples, we have selected *energetic particles* defined by two criteria: $\max[\gamma_i(t)] \geqslant 15\Theta_0$ and $\max[\gamma_i(t)] - \min[\gamma_i(t)] \geqslant 10\Theta_0$. Let $d\gamma_i(t) = (q_i/mc)(\boldsymbol{\beta}_i \cdot \boldsymbol{E}_i)(t)\,dt$ represent the instantaneous energy change of the ith particle between the times t and $t + dt$, where $q_i = \pm e$ is the particle charge. The corresponding contributions from perpendicular and parallel electric fields are $d\gamma_{i,\perp}(t) = (q_i/mc)(\boldsymbol{\beta}_i \cdot \boldsymbol{E}_{i,\perp})(t)dt$ and $d\gamma_{i,\parallel}(t) = (q_i/mc)(\boldsymbol{\beta} \cdot \boldsymbol{E}_{i,\parallel})(t)\,dt$, respectively. The total energy

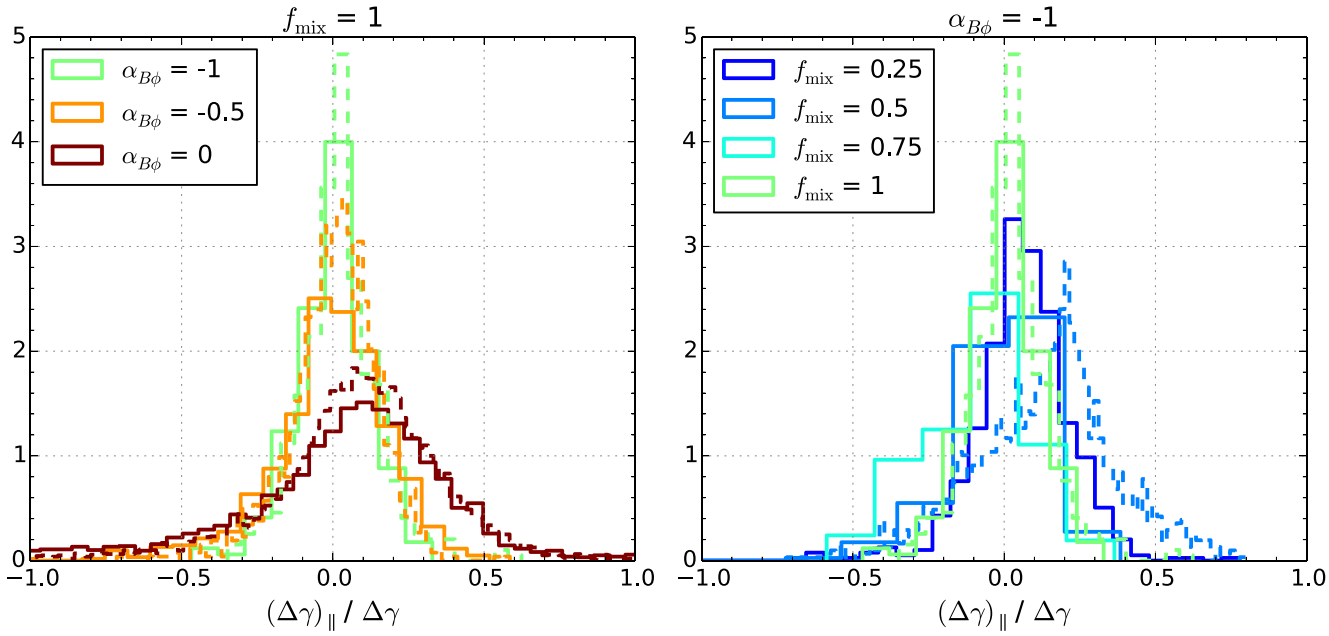

Figure 15. Distributions of the relative contribution $(\Delta\gamma)_\parallel$ of the electric field component $\boldsymbol{E}_\parallel$ parallel to the local magnetic field to the total energy gain $\Delta\gamma$ for complete samples of energetic particles. The line types are the same as in Figure 12.

gain of the ith particle has been calculated as $\Delta\gamma_i = \int_{t=0}^{t_{{\rm peak},i}} d\gamma_i$, interrupting the integration at the moment $t_{{\rm peak},i}$ at which the particle energy $\gamma_i(t)$ attains a global peak. The corresponding energy gains due to the perpendicular and parallel electric fields are $\Delta\gamma_{i,\perp} = \int_{t=0}^{t_{{\rm peak},i}} d\gamma_{i,\perp}$ and $\Delta\gamma_{i,\parallel} = \int_{t=0}^{t_{{\rm peak},i}} d\gamma_{i,\parallel}$, respectively.

Figure 15 compares the distributions of the $\Delta\gamma_{i,\parallel}/\Delta\gamma_i$ ratio for multiple simulations. In most cases, the distributions peak at $\Delta\gamma_{i,\parallel} \simeq 0$, which means that particle acceleration is dominated by perpendicular electric fields. However, in the f05_α-1_ξ100 case, the distribution peaks at $\Delta\gamma_{i,\parallel} \simeq 0.2\Delta\gamma_i$. Additional analysis of this case reveals various and complex histories of individual energetic particles that attain this level of parallel acceleration, an example of which will be presented further in this subsection. In the cases of $f_{\rm mix} = 1$ and $\alpha_{B\phi} = 0$, the distributions of $\Delta\gamma_{i,\parallel}$ peak at $\simeq 0.1\Delta\gamma_i$. Here, the reason is the relatively long duration of the initial simulation phase when random fluctuations of electric field contribute roughly equally to $\Delta\gamma_{i,\parallel}$ and $\Delta\gamma_{i,\perp}$.

Figure 16 compares the relative contributions of perpendicular electric fields to the energization of particles as a function of simulation time for the cases of $\alpha_{B\phi} = -1$ with different values of $f_{\rm mix}$ and ξ_n. These contributions have been summed over the samples of energetic particles as $S_\perp(t) = \sum_i d\gamma_{i,\perp}^2(t)$ and $S_\parallel(t) = \sum_i d\gamma_{i,\parallel}^2(t)$ (summing over energy squares greatly reduces the noise), and the relative contribution has been calculated as $s_\perp(t) = S_\perp(t)/[S_\perp(t) + S_\parallel(t)]$. Initially, for $t \lesssim L/c$, before the fast magnetic dissipation phase, when particle energy changes are limited to small random fluctuations, we find $s_\perp \sim 0.5$. With the onset of the fast magnetic dissipation phase, the relative contribution of perpendicular acceleration increases to $s_\perp \sim 0.95$, followed by a slow irregular decrease to the level of $s_\perp \sim 0.6$–0.8. As far as we can say, these results are not sensitive to the density ratio ξ_n, but they seem to depend on the pressure mixing parameter $f_{\rm mix}$ in the nonlinear phase. For $4.0 < ct/L < 4.5$, when the $s_\perp(t)$ functions for $f_{\rm mix} < 1$ achieve broad local minima, the highest relative contribution of perpendicular acceleration is $s_\perp \simeq 0.8$ for $f_{\rm mix} = 0.25$, and the lowest is $s_\perp \simeq 0.6$ for $f_{\rm mix} = 0.75$.[14] This dependence appears to be driven by differences in $S_\perp$ values (during that time, it is higher by a factor of $\simeq$5 in the $f_{\rm mix} = 0.25$ case, compared to the $f_{\rm mix} = 0.75$ case), rather than by differences in $S_\parallel$ values (higher by only $\simeq$50% for the same comparison).

We have searched the sample of energetic particles in the simulation f05_α-1_ξ100 for an illustrative example of significant contribution of parallel electric fields. Figure 17 shows the acceleration history of an energetic positron (denoted as "pos #930" or with subscript "930"), which is characterized by an initial energy of $\gamma_{930,{\rm ini}} \simeq 7.1\Theta_0$, and by $ct/L \simeq 3.5$ it reaches a peak energy of $\gamma_{930,{\rm peak}} \simeq 25.9\Theta_0$, hence $\Delta\gamma_{930} \simeq 18.8\Theta_0 \simeq 0.42\gamma_{\rm lim} \simeq 2.6\gamma_{930,{\rm ini}}$, of which $\simeq$25% is the contribution from parallel electric fields. Systematic acceleration by parallel electric fields with $\boldsymbol{E}\cdot\boldsymbol{B} \sim 0.005B_0^2$ is observed mainly in the period of $2.5 < ct/L < 2.95$.[15] During this time, the total electric field strength at the position of this particle is $|\boldsymbol{E}| \sim (0.1$–$0.2)B_0 \sim (0.3$–$0.5)|\boldsymbol{B}|$. As it happens, these are not the strongest electric fields that this particle experiences. At $t \simeq 2.4\,L/c$, the corresponding values are $\boldsymbol{E}\cdot\boldsymbol{B} \simeq -0.008B_0^2$ and $|\boldsymbol{E}| \simeq 0.3B_0 \simeq 0.58|\boldsymbol{B}|$. At that time, our particle experiences rapid acceleration, but the contribution of parallel electric fields up to that point is not important.

Figure 18 provides a detailed context for the parallel acceleration of positron #930. This particle is located not far from the central axis ($r \simeq 1.5R_0$), within a large patch of positive $\boldsymbol{E}\cdot\boldsymbol{B}$. Additional analysis shows that this particle interacts with the same patch for the entire period of parallel acceleration while propagating along a helical trajectory (since the dominant magnetic field components are still B_z and B_ϕ). In the (x,y) plane following the particle along the z coordinate,

[14] The case f05_α-1_ξ10 also achieves $s_\perp \simeq 0.6$, but only for $ct/L > 6$.

[15] This period of time coincides with the second phase of rapid increase of the maximum particle energy $\gamma_{\rm max}$ in this simulation, taking it beyond the $\gamma_{\rm lim}$ limit (see the dashed blue line in the right panel of Figure 12).

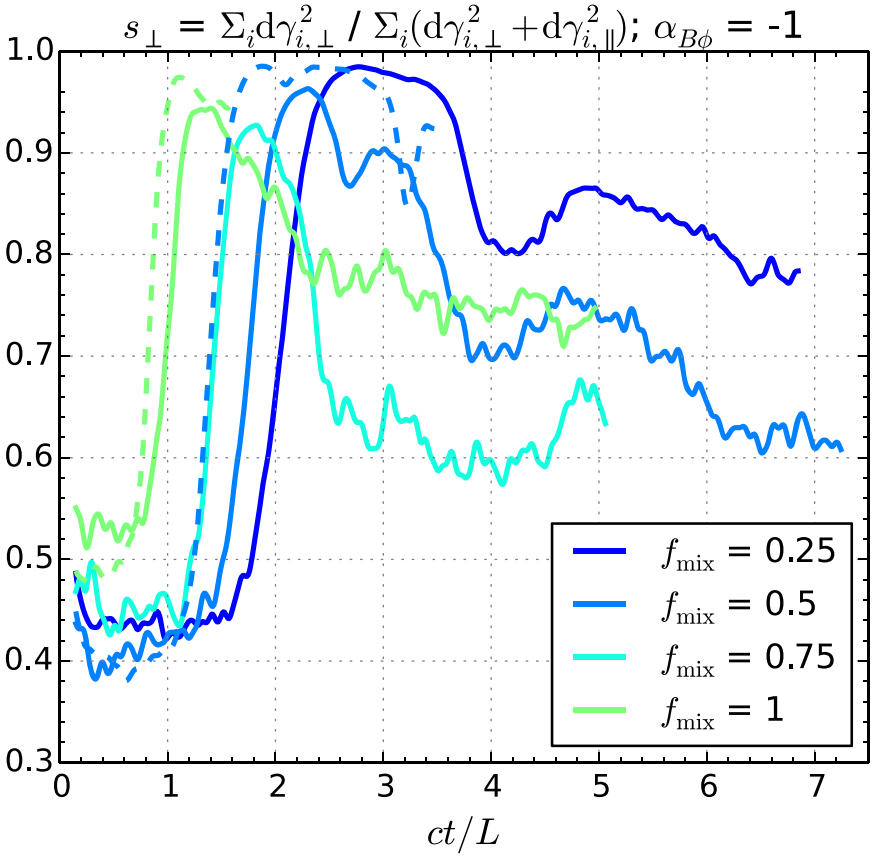

Figure 16. Relative contribution of perpendicular electric fields to the squared energy gains of energetic particles (using the formula shown in the plot title) as a function of simulation time for simulations with $\alpha_{B\phi} = -1$ and different values of $f_{\rm mix}$ (indicated by the line color) and ξ_n (indicated by the line type, same as in Figure 12).

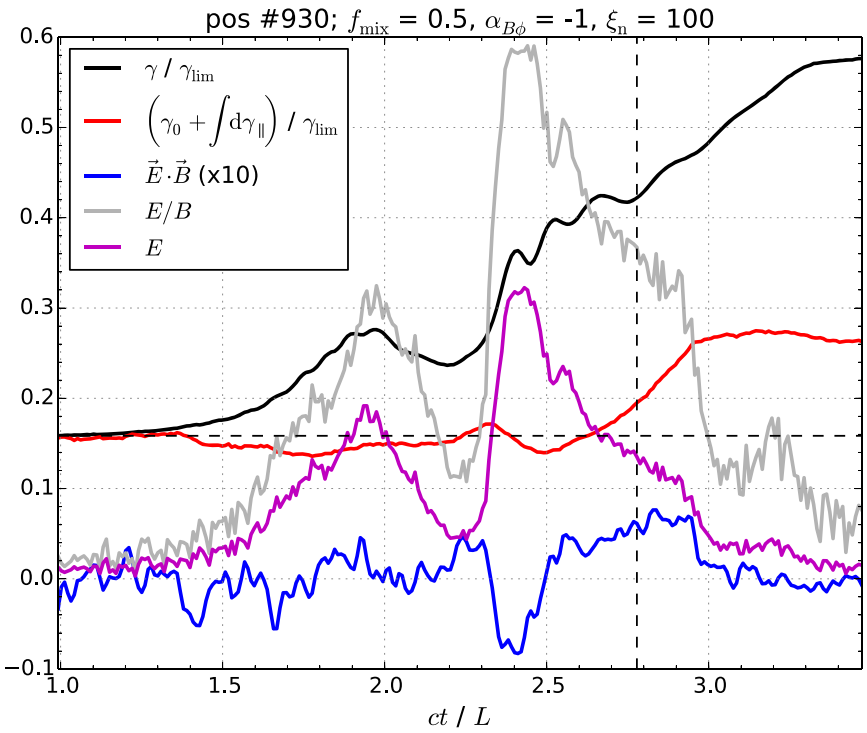

Figure 17. Acceleration history of the energetic positron #930 in the simulation f05_α-1_ξ100 that shows a significant contribution of parallel electric fields to its acceleration, with $\Delta\gamma_{i,\parallel} \simeq 0.25\Delta\gamma_i$. The black solid line shows the particle energy $\gamma_i(t)$, and the red solid line shows the integrated contribution of parallel electric fields $\gamma_i(t=0) + \int d\gamma_{i,\parallel}$, both normalized to $\gamma_{\rm lim}$. The magenta, gray, and blue solid lines show the local values of $|\boldsymbol{E}|$, $|\boldsymbol{E}|/|\boldsymbol{B}|$, and $(\boldsymbol{E}\cdot\boldsymbol{B}) \times 10$, respectively. The vertical dashed line indicates the moment presented in Figure 18.

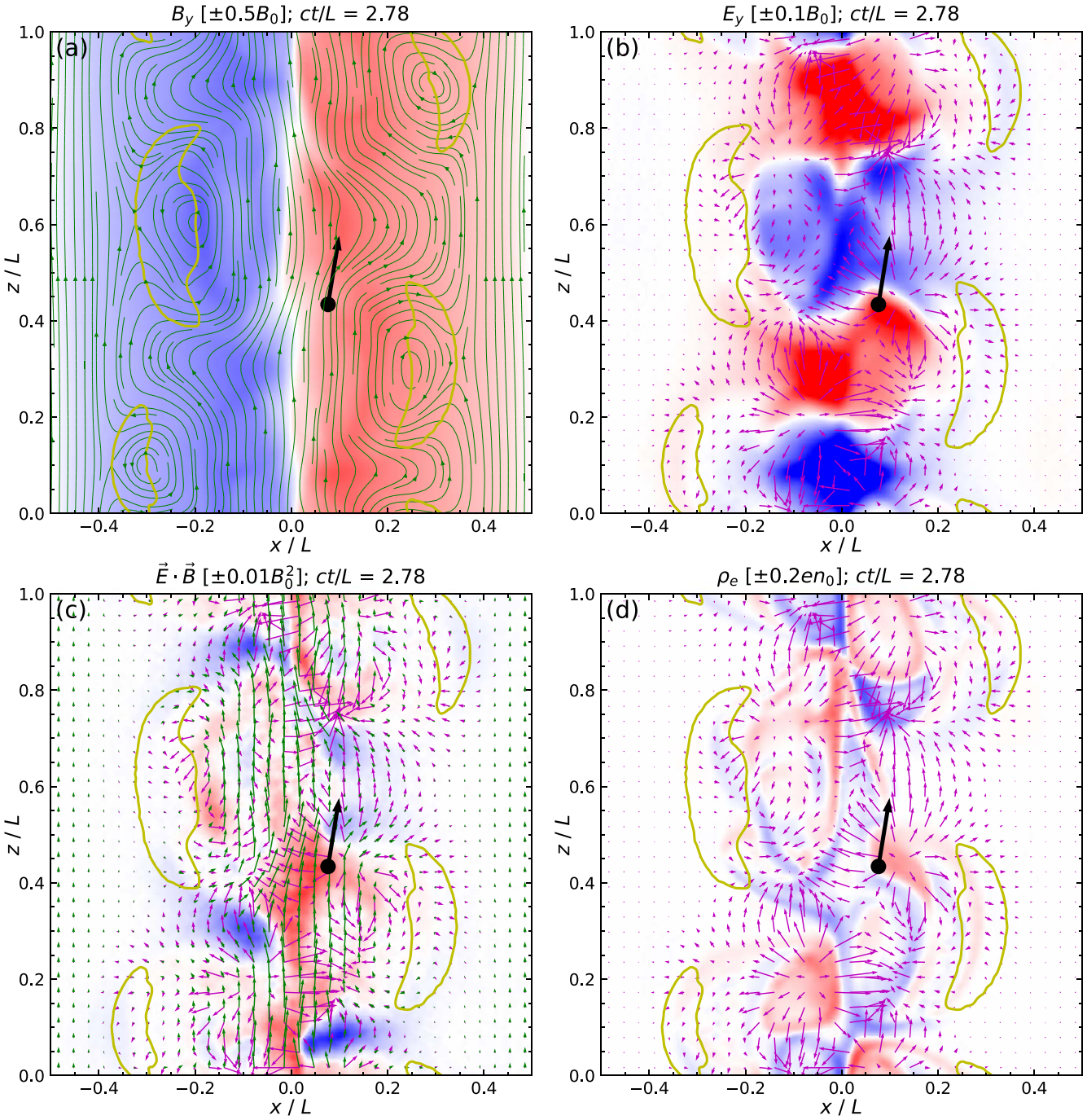

Figure 18. A snapshot from the simulation f05_α-1_ξ100 at the time $t = 2.78\ L/c$, when the energetic positron #930 introduced in Figure 17 (marked with the black circles, with the black arrows indicating the in-plane velocity direction) experiences systematic acceleration by electric field parallel to the local magnetic field. Each panel shows an (x,z) map in the $y = 0$ plane, which also contains the energetic positron. The color maps (red is positive, blue is negative) show: (a) out-of-plane magnetic field component B_y, (b) out-of-plane electric field component E_y, (c) $\boldsymbol{E}\cdot\boldsymbol{B}$, and (d) charge density ρ_e. The magenta vector fields show the in-plane electric field (E_x, E_z), and the green vector field (panel (c)) shows the in-plane magnetic field (B_x, B_z). Panel (a) also includes a streamplot of (B_x, B_z) with solid green lines. The yellow contours indicate where $B_z = 0$.

the patch is seen to rotate around the central axis, and the particle motion appears to be synchronized with this rotation. The origin of that $\boldsymbol{E}\cdot\boldsymbol{B} > 0$ patch is discussed in Section 6.1.

5.3. Relation to Current Density and Electric Field Structures

We have considered the possible relation between acceleration of energetic particles and their location with respect to structures of current density and electric field. In general, this is a very complex problem, because it requires characterizing a small sample of individual particles that succeed in achieving high energies by interacting with dynamical 3D electric fields and currents. We are attempting to illustrate this relation with only a few snapshots out of many that we have produced and examined.

Figure 19 presents single snapshots for two simulations (f025_α-1_ξ10 and f1_α-1_ξ100, chosen because they probe different values of $f_{\rm mix}$ and produce relatively large samples

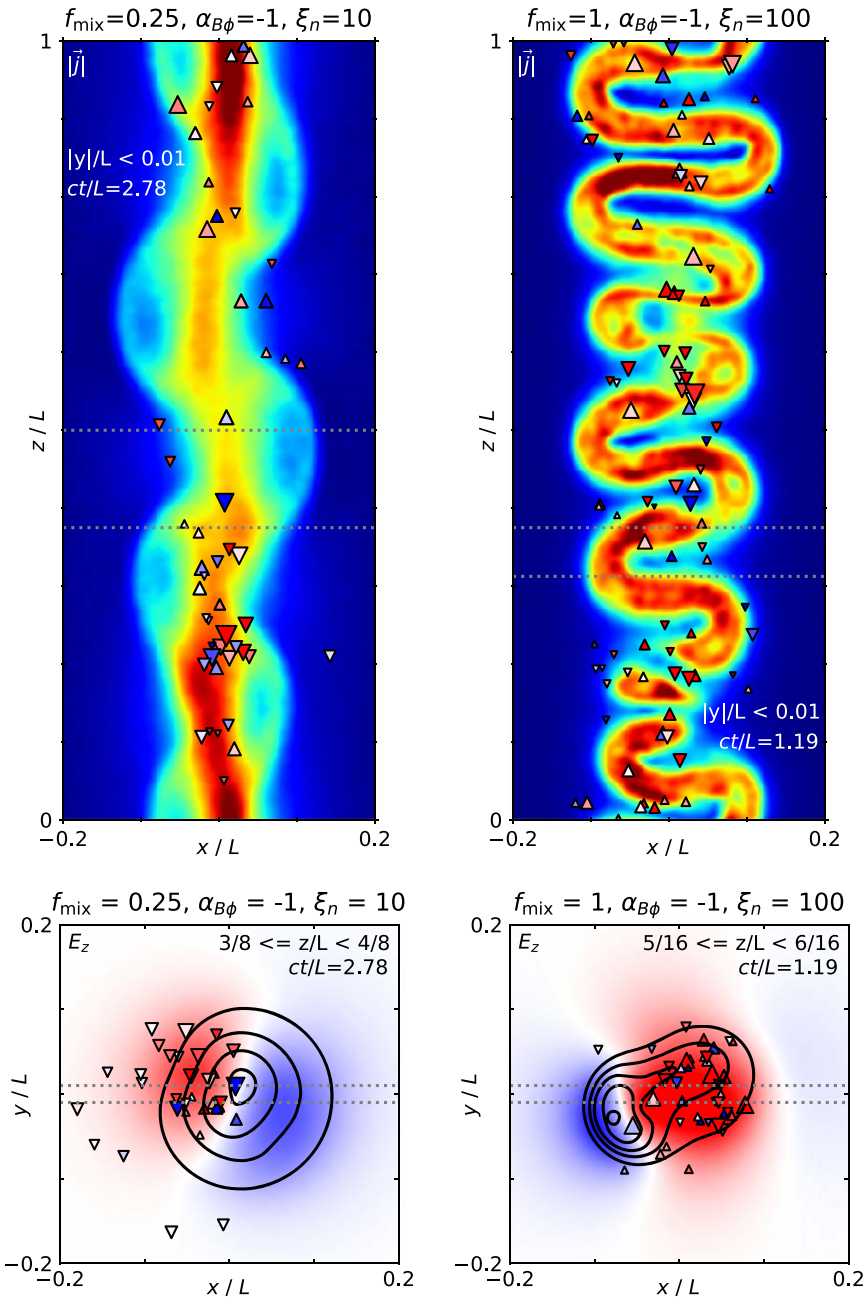

Figure 19. The *upper panels* show (x,z) maps of total current density $|\boldsymbol{j}|$ (arbitrary units; the color scale is the same as in Figure 5) in the $y/L \simeq 0$ plane for the simulations f025_α-1_ξ10 (see the left panel of Figure 8) and f1_α-1_ξ100. The symbols indicate the positions of individual energetic particles: upward-pointing triangle represent the positrons, downward-pointing triangles represent the electrons, the sizes indicate the current particle energy, and the colors indicate the current particle energization rate (red means energy gain, blue means energy loss). The gray dotted lines indicate the range of z used for integrating the (x,y) maps shown below. The *lower panels* show (x,y) maps of axial electric field E_z (red means $E_z > 0$, blue means $E_z < 0$) averaged over the indicated range of z/L. The gray dotted lines indicate the range of y used for integrating the (x,z) maps shown above.

of energetic particles), each illustrated by an (x,z) map (in the $y/L \simeq 0$ plane) of total current density $|\boldsymbol{j}|$, and by an (x,y) map (averaged over a range of z/L) of axial electric field E_z with overlaid contours of $|\boldsymbol{j}|$. In all maps, we indicate the locations, energies, and acceleration rates of individual particles that are present in the probed volume regions and that are going to become energetic (according to the definition given in Section 5.2).

One question that we are attempting to address is whether there are thin current layers that could be sites of magnetic reconnection. We find in general that structures of current density are not sharp on kinetic scales ($\sim \rho_0$). A particularly complex meandering (x,z) structure of $|\boldsymbol{j}|$ can be seen in the f1_α-1_ξ100 simulation; it results from an initially cylindrical current core being sheared while retaining its initial thickness scale ($\sim R_0$).

Another question is whether the locations of energetic particles are correlated with these current density structures. We do not find any evidence for that. However, the (x,y) maps suggest that energetic particles are preferentially located in regions of $E_z > 0$ while avoiding regions of $E_z < 0$. We know already from Figure 8 that there is no symmetry between

regions of positive and negative E_z. The former ($E_z > 0$) dominate and are better connected, which allows local particles to spend more time in these acceleration zones. We thus find that the locations of particles undergoing successful acceleration are related more strongly to the structures of electric field, rather than current density.

6. Discussion

The first motivation for this project has been to bridge the diverse magnetic pinch configurations investigated recently with 3D kinetic numerical simulations: the Z-pinch case (with the toroidal magnetic fields balanced entirely by the gas pressure) studied by Alves et al. (2018, 2019) and the FF screw-pinch case (with the toroidal magnetic fields balanced entirely by the axial magnetic field) studied by Davelaar et al. (2020). To this end, we introduced the pressure mixing parameter $f_{\rm mix}$ such that $f_{\rm mix} = 0$ corresponds to the FF screw-pinch limit, and $f_{\rm mix} = 1$ corresponds to the Z-pinch limit. This allowed us to investigate the effect of $f_{\rm mix}$ for exactly the same radial profiles of toroidal magnetic field $B_\phi(r)$. In the case $f_{\rm mix} = 0$, we have found particle acceleration to be inefficient, with $\gamma_{\rm max}$ increasing by only $\simeq$10% (see Figure 12; note that this simulation ran until $t \simeq 15\,L/c$ without any further increase of $\gamma_{\rm max}$). A key difference from the setup of Davelaar et al. (2020) is that they initialized the plasma as relativistically cold with $\Theta_0 = 10^{-2}$, and our plasma is initialized as relativistically hot with $\Theta_0 = 10^4$. In their simulations, particles reach Lorentz factors $\gamma \sim \sigma$ with magnetizations $\sigma \sim 10$–40. In our case $f_{\rm mix} = 0$, we have peak magnetization of only $\sigma_{\rm hot}(r = 0) \simeq 2.8$, much less than the initial Maxwell–Jüttner value of $\gamma_{\rm max}/\Theta_0 \simeq 20$; we think that this is the reason for the inefficient particle acceleration. Nevertheless, we achieve higher initial magnetizations (see the right panels of Figure 1), and hence efficient particle acceleration, in other cases. Already for $f_{\rm mix} = 0.25$ (and higher), the most energetic particles achieve the Hillas-type energy limit $\gamma_{\rm lim}$ introduced by Alves et al. (2018).

Our second motivation has been to include a flexible power-law section in the radial profile of toroidal magnetic field $B_\phi(r)$. Both Alves et al. (2018, 2019) and Davelaar et al. (2020) investigated steeply decaying $B_\phi(r)$ profiles beyond the core radius R_0. In the case of Alves et al. (2018, 2019), it was an exponential tail $B_\phi(r \gg R_0) \propto \exp(-r/R_0)$, and in the case of Davelaar et al. (2020), it was a family of profiles with approximately $\propto r^{-1}$ tails (see the left panel of Figure 1). In the Z-pinch limit ($f_{\rm mix} = 1$), the analytical predictions of Begelman (1998) and Das & Begelman (2019) are that power-law profiles $B_\phi(r) \propto r^{\alpha_{\rm B}\phi}$ should be locally unstable for $\alpha_{\rm B}\phi > -1$. Such shallow-decay (or even flat) profiles of $B_\phi(r)$ have not been studied before by means of kinetic simulations.[16]

Despite the modest numerical scale separation of our simulations, we were able to confirm most of the previous results, especially those of Alves et al. (2018) in the Z-pinch limit—the structure of electric fields in the linear instability phase and the existence of the particle energy limit $\gamma_{\rm lim}$. In the case of shallow $B_\phi(r)$ profiles ($\alpha_{\rm B}\phi > -1$), this limit needs to be redefined to $(R_{\rm B}\phi/R_0)\gamma_{\rm lim}$, introducing a new characteristic radius $R_{\rm B}\phi(\alpha_{\rm B}\phi) > R_0$. In Section 2, we suggested preliminary values of this radius: $R_{\rm B}\phi \simeq 1.55R_0$ for $\alpha_{\rm B}\phi = -0.5$, and $R_{\rm B}\phi \simeq 2.5R_0$ for $\alpha_{\rm B}\phi = 0$. However, our simulations for $\alpha_{\rm B}\phi > -1$ had to be interrupted early, since the perturbations reached the domain boundaries before the fast magnetic dissipation phase and the associated particle acceleration were complete. Simulating a complete fast magnetic dissipation phase would require, e.g., shifting the outer cutoff to an intermediate radius.

We argue that the particle energy limit $\gamma_{\rm lim}$ should not be interpreted as resulting directly from particle confinement by toroidal magnetic fields, because we have not found any example of an energetic particle (out of 6×10^5 individually tracked particles per simulation), the acceleration of which would be interrupted by its escape from the inner radii. Efficient particle acceleration coincides with the fast magnetic dissipation phase, which in the cases of $\alpha_{\rm B}\phi \leqslant -1$ is of well-defined duration, and is also confined to the inner region of $r \lesssim 2R_0$ (see Figures 3 and 5). However, in the cases of $\alpha_{\rm B}\phi > -1$, magnetic dissipation can propagate to larger radii ($r > 2R_0$) and induce widespread and sustained electric fields.

In the most extreme Z-pinch case f1_α0_ξ100, which provides the highest magnetization in the outer regions, we find a weak signature of a local pinch mode at the intermediate radii of (5–7)$R_0 \simeq R_{\rm out}/2$ (see Figure 5). This is the first numerical confirmation that the Z-pinch modes identified analytically by Begelman (1998) can be truly local in the sense that $k_z r_{\rm c} \gg 1$ and $\sigma_r \ll r_{\rm c}$ (for a mode centered at $r = r_{\rm c}$ with radial dispersion σ_r; this was predicted in the linear limit by Das & Begelman 2019). The fact that this mode has been identified in this particular case at these particular radii is consistent with the solutions of the local dispersion relation of Begelman (1998) presented in Figure 20 and described in Appendix B. That weak local mode is eventually dominated by a stronger pinch mode propagating outward from the central core region.

6.1. Parallel versus Perpendicular Acceleration

Particle acceleration by parallel electric fields in strongly magnetized jets with axial magnetic flux has been demonstrated by Davelaar et al. (2020), who attribute these fields to magnetic reconnection. They show examples of magnetic X-points in the (x,z) plane along the outer fronts of perturbation, where the axial magnetic field component is reversed on the perturbation side ($B_z < 0$), interacting with $B_z > 0$ in the unperturbed medium, as well as other magnetic irregularities in the (x,y) plane.

Such X-points can be seen clearly in our simulation f05_α-1_ξ100, where Figure 18(a) shows closed yellow contours in the (x,z) plane, along which $B_z = 0$, meaning that $B_z > 0$ outside (like in the entire domain in the initial configuration) and $B_z < 0$ inside. We also show using the `matplotlib.pyplot.streamplot` tool (which by default does not illustrate the field strength) that the inner (with respect to the central axis) sections of those contours include a magnetic O-point in the (x, z) plane, and the outer sections include a magnetic X-point, as has been shown by Davelaar et al. (2020). These magnetic X-points are potential sites of magnetic reconnection. Since the $B_y \equiv B_\phi$ component is smooth across the X-points (a finite guide field $B_{\rm g}$), one would expect the reconnection-induced nonideal out-of-plane electric field to have a component parallel to the local magnetic field. However, Figure 18 shows that E_y is very weak along the outer sections of the $B_z = 0$ contours, and moreover, that $\boldsymbol{E} \cdot \boldsymbol{B}$ is also insignificant there, as compared

[16] A "sinusoidal" profile of $B_\phi(r) \propto [1 - \cos(2\pi r/R_{\rm out})]$ that was investigated with RMHD simulations by O'Neill et al. (2012) is included in the left panel of Figure 1. It has a symmetry similar to that of our case $\alpha_{\rm B}\phi = 0$, but very different asymptotics at $r < R_0$.

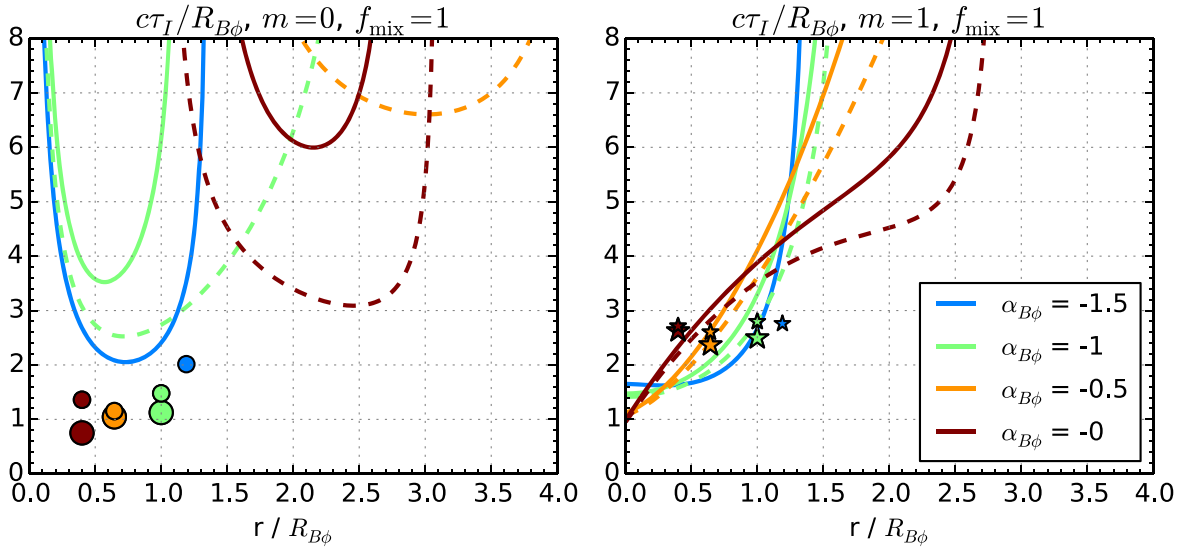

Figure 20. Growth timescales $\tau_{\rm I}$ of the local instability modes for the initial configurations of the $f_{\rm mix}=1$ Z-pinch cases calculated according to the dispersion relation of Begelman (1998). The left panel shows the results for the $m=0$ pinch mode, and the right panel shows the results for the $m=1$ kink mode. The line colors indicate the value of $\alpha_{\rm B\phi}$. The solid lines correspond to $\xi_n=10$, and the dashed lines correspond to $\xi_n=100$. Minimum growth timescales $c\tau_{\rm min}/R_{\rm B\phi}$ measured at the $1<r/R_0<2$ shell region of our simulations are indicated at $r=R_0$ using the same symbols as in Figure 7 (the smaller symbols correspond to $\xi_n=10$ and the larger ones to $\xi_n=100$).

with the inner regions. We have also checked the total nonideal electric field $\boldsymbol{E}_{\rm nonid}$ and the current density $\boldsymbol{j}$, finding that they are all very weak at the magnetic X-points. We therefore conclude that these magnetic X-points are not sites of active magnetic reconnection. Note that the relative strength of the reconnecting field component is $|B_z|\sim 0.2|B_\phi|$ inside the $B_z=0$ contours, which corresponds to a very strong guide field of $B_{\rm g}\sim 5|B_z|$, sufficient to suppress magnetic reconnection and particle acceleration (e.g., Dahlin et al. 2016; Werner & Uzdensky 2017, 2021).

Let us also discuss the origin of the positive $\boldsymbol{E}\cdot\boldsymbol{B}$ region that accelerates positron #930 in the nonlinear stage of simulation f05_α-1_ξ100, presented in Figure 18 and described in Section 4.2. Additional analysis reveals that nonzero $\boldsymbol{E}\cdot\boldsymbol{B}$ first appears during the saturation of the linear instability stage around $t\simeq 1.8\,L/c$, with positive $\boldsymbol{E}\cdot\boldsymbol{B}$ aligned with the deformed column of strong electric current, and with negative $\boldsymbol{E}\cdot\boldsymbol{B}$ outside that column. In this simulation, we also observe a second generation of the linear central instability, starting at $t\simeq 2.3\,L/c$, which is evidenced in the history of the energetic positron #930 (Figure 17) as a major increase of the total electric field following that moment. This second instability also generates the inner structures of charge density (within $-0.15<x/L<0.15$) that can be seen in the lower right panel of Figure 18. We conjecture that the centrally located patch of positive $\boldsymbol{E}\cdot\boldsymbol{B}$ seen for $2.5<ct/L<2.95$ results from the nonlinear saturation of the second-generation instability. The energetic positron #930 experiences the most efficient parallel acceleration because it happens to interact with that patch for as long as possible.

6.2. Instability Growth Timescales

In the FF case $f_{\rm mix}=0$, the measured minimum instability timescales $\tau_{\rm min}$ reported in the right panel of Figure 7 can be compared with the analytical predictions of Appl et al. (2000). In the case of constant magnetic pitch $\mathcal{P}_0=R_0$, the shortest growth timescale is theoretically predicted for the $|m|=1$ kink mode: $c\tau/R_0\simeq 7.52/\beta_{\rm A}\simeq 8.78$, where $\beta_{\rm A}\simeq 0.857$ is the Alfvén velocity at $r=0$ in our $f_{\rm mix}=0$ configuration. This is very close to our measurement of $c\tau/R_0\simeq 8.45$.[17] However, we also measure shorter timescales for the $m=0$ and $m=2$ modes in this case, which is inconsistent with the analytical predictions, according to which the pinch mode should be stable and the $m=2$ mode should have a longer growth timescale (and a wavelength that would hardly fit in our domain). This suggests that the measured $m=0$ and $m=2$ modes are not linear, but instead they are secondary modes triggered nonlinearly by the linear kink mode. This interpretation is supported by the fact that the onsets of the $m=0$ and $m=2$ modes are delayed with respect to the onset of the kink mode, and this is actually evident in most other cases reported in Figure 6.

In the Z-pinch cases of $f_{\rm mix}=1$, the measured values of $\tau_{\rm min}$ can be compared with the solutions of the local dispersion relation of Begelman (1998), reported in Figure 20 and described in Appendix B. Although the analytical solutions can be very steep functions of r, a fairly close agreement is found for the $m=1$ kink mode between the measured values extracted from the $1<r/R_0<2$ shell and the theoretical solutions evaluated at $r=R_0$. For the $m=0$ pinch mode, the measured values are shorter than the theoretical solutions even for $\alpha_{\rm B\phi}\leqslant -1$. This again suggests that only the kink mode measured in our simulations is linear.

6.3. Astrophysical Implications

The potential for development of instabilities due to toroidal magnetic field has been an important question in the theoretical picture of magnetized astrophysical jets.

The toroidal component of ordered magnetic fields is an essential ingredient of relativistic jets. As the jets are rooted in rotating structures (e.g., spinning black holes), toroidal fields are generated by azimuthal shearing of poloidal fields. These provide the magnetic pressure that accelerates the jet, and they

[17] The corresponding analytical wavelength is $\simeq 8.43R_0$, very close to our effective wavelength of $\lambda_z\simeq 8.8R_0$ reported in Section 4.2.

carry the outgoing Poynting flux (e.g., Davis & Tchekhovskoy 2020). Toroidal fields provide a tension force that, in principle, would allow the jet to be collimated (pinched)[18] and to maintain a structure of radially decreasing (away from the jet axis) total pressure and energy density (e.g., Begelman et al. 1984). In the lateral jet expansion, toroidal fields decay more slowly than poloidal fields, hence the pinching effect of toroidal fields can be expected to increase with distance along the jet (e.g., Bogovalov & Tsinganos 1999).

The relative importance of current-driven and pressure-driven modes in astrophysical jets depends crucially on the strength, lateral distribution, and evolution along the jet of the poloidal magnetic field. Davelaar et al. (2020) argued that FF configurations with significant poloidal fields are naturally expected in the relativistic jets emerging from the bulk-acceleration and collimation zone, protected from external modes by the lack of causal contact across the jet (Bromberg & Tchekhovskoy 2016; Tchekhovskoy & Bromberg 2016). Causality would be regained due to recollimation once the external pressure becomes important, and that would make FF jets unstable, at first to the current-driven modes.

It should be noted, however, that whether causality is lost in a relativistic jet depends on the scaling of external pressure $P_{\rm ext}$ with distance z along the jet. Porth & Komissarov (2015) showed that causality is lost only when $P_{\rm ext}(z)$ is steeper than z^{-2}, and even in such cases the jet core can be pinched by toroidal magnetic field, triggering an internal instability.

In order for the Z-pinches to operate in jets, sufficient gas pressure needs to build up, presumably due to other heating mechanisms, e.g., internal shocks (e.g., Spada et al. 2001; Pjanka & Stone 2018), recollimation shocks (e.g., Bromberg & Levinson 2009; Nalewajko & Sikora 2009), magnetic reconnection due to global field reversals (e.g., Lovelace et al. 1997; Nalewajko et al. 2011; Giannios & Uzdensky 2019), or nonlinear saturation of the current-driven modes, in effect boosting their dissipation efficiency. Gas pressure can also be reduced by radiative cooling, especially in the jets hosted by powerful quasars and GRBs, or due to adiabatic expansion. This suggests that Z-pinches can only operate in the vicinity of gas pressure sources.

At any distance z along the jet, the strength of toroidal magnetic field must peak at some radius $R_{B\phi}$, which is intermediate when compared with the jet radius: $0 < R_{B\phi}(z) < R_{\rm j}(z)$. Our study shows that the $R_{B\phi}(z)$ function is of considerable interest, because it largely determines the minimum growth timescale $\tau_{\rm min}$ of the instabilities (see Figure 7). Let us then consider qualitatively the development of an initially FF jet—as it expands, internal pinching is expected to reduce the $R_{B\phi}/R_{\rm j}$ ratio. In the FF jet core, the instability growth timescale is roughly $\tau(z) \sim 9R_{B\phi}(z)/c$; it would evolve much slower than the jet crossing timescale $R_{\rm j}(z)/c$. It is then quite likely that this first instability will be able to evolve nonlinearly and to saturate. At this point, a fraction of the inner toroidal field will be dissipated, tending to increase $R_{B\phi}$, most likely in a fashion similar to the results shown in Figure 3 for two Z-pinch cases. Another effect of the first instability is generation of gas pressure, effectively increasing $f_{\rm mix}$, so that the jet core is no longer FF. If the gas pressure is significant compared with the axial magnetic pressure, it would reduce the instability growth timescale noticeably (Figure 7 shows that, for $f_{\rm mix} = 0.25$, the growth timescale of the kink mode is already reduced by $\sim$40% compared with the FF limit $f_{\rm mix} = 0$). The overall outcome of this scenario depends on the relative importance of: (1) pinching of the jet core by outer toroidal fields, (2) dissipation of the inner toroidal fields, and (3) production of gas pressure. This problem should be addressed by future numerical simulations of initially FF jets with a significantly larger separation of scales L/R_0.

We have also demonstrated numerically the presence of a weak pinch mode localized at intermediate radii in the case $f_{\rm mix} = 1$ and $\alpha_{B\phi} = 0$, as predicted by Begelman (1998) and Das & Begelman (2019). Such local modes can operate in the outer jet regions even when their cores are relatively stable. In particular, flat $B_\phi(r)$ profiles, decreasing with r more slowly than r^{-1} ($\alpha_{B\phi} > -1$), would be susceptible to these modes. Such flat $B_\phi(r)$ profiles may develop in relativistic jets at large distances, as was found in global 3D RMHD simulations by Bromberg & Tchekhovskoy (2016).[19]

7. Conclusions

We have presented the results of 3D kinetic numerical simulations of cylindrical static jets with toroidal magnetic fields in relativistic pair plasma. Our simulations were initiated from configurations based on power-law profiles of $B_\phi(r) \propto r^{\alpha_{B\phi}}$, with the toroidal field index $-1.5 \leqslant \alpha_{B\phi} \leqslant 0$, modified by inner and outer cutoffs. The toroidal field was balanced by a combination of axial magnetic field $B_z(r)$ and gas pressure $P(r)$, whose relative importance was parameterized by the pressure mixing parameter $0 \leqslant f_{\rm mix} \leqslant 1$, such that $f_{\rm mix} = 0$ corresponds to the force-free screw-pinch case with uniform gas pressure, and $f_{\rm mix} = 1$ corresponds to the Z-pinch case with $B_z(r) = 0$. The initial hot magnetizations were up to $\sigma_{\rm hot} \simeq 8$ locally.

We found that all investigated cases were unstable, with the $m = 1$ kink mode being either dominant (for $f_{\rm mix} < 1$) or comparable to the $m = 0$ pinch mode (for $f_{\rm mix} = 1$). The minimum linear growth timescale $\tau_{\rm min}$ for the kink mode in E_z, as well as the effective axial wavelength λ_z, were found to decrease systematically with increasing $f_{\rm mix}$. In the case $f_{\rm mix} = 1$ and $\alpha_{\rm B\phi} = 0$, we have found a weak $m = 0$ pinch mode localized at intermediate radial distances, consistent with the local dispersion relation of Begelman (1998).

These instabilities are associated with dissipation of toroidal magnetic flux $\Psi_{B\phi}$, which typically proceeds in two phases: a fast magnetic dissipation phase followed by a slow one. The fast magnetic dissipation phase drives efficient particle acceleration. For shallow toroidal field profiles ($\alpha_{B\phi} \geqslant -0.5$), magnetic dissipation proceeds more slowly, and the fast magnetic dissipation phase is typically not complete before the perturbations reach the outer boundaries.

Particle acceleration is dominated by electric fields perpendicular to the local magnetic fields. Acceleration by parallel electric fields is possible in the central core region ($r < R_0$) in the presence of axial magnetic fields ($f_{\rm mix} < 1$); however, strong guide fields suppress the efficiency of magnetic reconnection in the outer regions. While current density $|\boldsymbol{j}|$ forms complex volumetric structures, we have not identified

[18] Although, in the acceleration stage of relativistic jets, collimation by external pressure is more important in determining the final jet opening angle (Tchekhovskoy et al. 2010; Komissarov et al. 2010).

[19] However, it appears that instability is suppressed in that case by a strong poloidal field (Das & Begelman 2019).

kinetically sharp current layers. For steep toroidal field profiles ($\alpha_{B\phi} \leqslant -1$), the most energetic particles reach the confinement energy limit $\gamma_{\rm lim} = eB_0R_0/mc^2$. On the other hand, for shallow toroidal field profiles ($\alpha_{B\phi} \geqslant -0.5$), the most energetic particles approach a rescaled energy limit of $(R_{B\phi}/R_0)\gamma_{\rm lim}$, where $R_{B\phi}$ is related to the peak radius of the initial $B_\phi(r)$ function ($R_{B\phi} = R_0$ for $\alpha_{B\phi} = -1$).

We have thus confirmed most of the results of previous kinetic simulations in the Z-pinch limit (Alves et al. 2018) and in the FF screw-pinch limit (Davelaar et al. 2020). These previous studies represent two special cases among many possible internal jet configurations. In contrast, our work is more general, as we have demonstrated how these previous results can be bridged by investigating the cases of mixed pressure balance. Thanks to the capabilities of the `Zeltron` code (Cerutti et al. 2013), this investigation can be extended to include the effect of radiative cooling due to synchrotron and inverse Compton processes on particle acceleration (Nalewajko et al. 2018; Werner et al. 2019; Zhdankin et al. 2020), and to calculate the radiative output including multiwavelength light curves and linear polarization (Yuan et al. 2016). This could potentially identify a unique signature of these instabilities in the vast observational data on blazars (e.g., Madejski & Sikora 2016), a subclass of AGNs dominated by nonthermal emission from relativistic jets.

These results are based on numerical simulations performed at the supercomputer `Prometheus` located at the Academic Computer Centre "Cyfronet" of the AGH University of Science and Technology in Krakow, Poland (PLGrid grants `pic19`, `plgpic20`,`plgpic21`,`ehtsim`); and at the computing cluster `Chuck` located at the Nicolaus Copernicus Astronomical Center of the Polish Academy of Sciences in Warsaw, Poland. This work was supported by the Polish National Science Centre grants 2015/18/E/ST9/00580 and 2021/41/B/ST9/04306, and by the U.S. National Science Foundation grants AST 1903335 and AST 1806084. B.M. acknowledges support from DOE through the LDRD program at LANL and from the NASA Astrophysics Theory Program.

Appendix A
Particle Confinement by Toroidal Magnetic Field

Consider a radial profile of toroidal magnetic field $B_\phi(r)$ in the form given by Equation (4), but without an outer cutoff. In the absence of electric fields, a relativistic particle of mass m, charge $q = \pm e$, constant Lorentz factor $\gamma \gg 1$, dimensionless velocity $\boldsymbol{\beta} = \boldsymbol{v}/c = [\beta_r, \beta_\phi, \beta_z]$ (parameterized as $\beta_r \simeq \sin\theta$, $\beta_\phi = 0$, $\beta_z \simeq \cos\theta \equiv \mu$), and momentum $\boldsymbol{p} = \gamma\boldsymbol{\beta}mc$ would propagate under the Lorentz force $d\boldsymbol{p}/dt = q(\boldsymbol{\beta} \times \boldsymbol{B}) = qB_\phi(r)[-\cos\theta, 0, \sin\theta]$. Noting that $d\boldsymbol{p}/dt = \gamma mc(d\boldsymbol{\beta}/dt) = \gamma mc^2\beta_r(d\boldsymbol{\beta}/dr) = \gamma mc^2\beta_r$[cos and $d\mu/dr = -\sin\theta(d\theta/dr)$, the particle trajectory can be described by the equation

$$\frac{d\mu}{d(r/R_0)} = \pm\left(\frac{\gamma}{\gamma_{\rm lim}}\right)^{-1}\frac{B_\phi(r)}{B_0}, \tag{A1}$$

where $\gamma_{\rm lim} = eB_0R_0/(mc^2)$. For $\alpha_{B\phi} = -1$, this equation can be solved analytically, yielding

$$\mu(r) = \mu_0 \pm \frac{1}{2}\left(\frac{\gamma}{\gamma_{\rm lim}}\right)^{-1}\ln\left[1 + \left(\frac{r}{R_0}\right)^2\right], \tag{A2}$$

where $\mu_0 = \mu(r = 0)$. In the specific case $q = +e$ (a positron), the maximum radius $r_{\rm max}$ is given by $\mu(r_{\rm max}) = 1$. If we adopt a confinement criterion $r_{\rm max} < r_{\rm conf}$, this can be expressed as

$$\gamma - u_{z,0} < \frac{\gamma_{\rm lim}}{2}\ln\left[1 + \left(\frac{r_{\rm conf}}{R_0}\right)^2\right], \tag{A3}$$

where $u_{z,0} \simeq \gamma\mu_0$ is the axial four-velocity component at $r = 0$. This criterion simplifies to $\gamma - u_{z,0} < \gamma_{\rm lim}$ for $r_{\rm conf} \simeq 2.53R_0$, which is a reasonable threshold. Note that $\gamma_{\rm lim}$ is relevant as the confinement energy limit only for particles with $u_{z,0} \simeq 0$, i.e., crossing the symmetry axis at the right angle. Particles propagating along the axis can reach energies beyond $\gamma_{\rm lim}$ without escaping. For analysis of acceleration histories of individual particles, we introduce the *particle confinement indicator* defined as $\xi_{\rm conf} = (\gamma - |u_z|)/\gamma_{\rm lim}$, so that a particle is considered confined if $\xi_{\rm conf} < 1$.

Appendix B
Linear Growth Timescales in the Z-pinch Cases

Instability growth timescales in the $f_{\rm mix} = 1$ Z-pinch cases can be calculated analytically using the local dispersion relation expressed by Eq. (3.32) of Begelman (1998) in the limit of $B_z = 0$ and $l \ll k$ (negligible radial wavenumber). The dispersion relation is solved for the initial equilibria used in our simulations as a function of radius r. Figure 20 presents the resulting exponential growth timescales $\tau_{\rm I} = 1/\omega_{\rm I}$ for the $m = 0$ pinch and $m = 1$ kink modes scaled by the characteristic radius $R_{{\rm B}\phi}$. Higher azimuthal modes are found to be stable in all considered cases. All configurations are unstable to the kink mode with the shortest growth timescales ($c\tau_{\rm I}/R_{{\rm B}\phi} \sim 1.0$–$1.6$) found within $r < R_{{\rm B}\phi}$. For $\alpha_{{\rm B}\phi} > -1$, the unstable region extends toward intermediate radii, up to $r \simeq 2.5R_{{\rm B}\phi}$ for the case f1_α0_ξ100, but with significantly longer growth timescales. The solutions are more diverse for the pinch mode—the central core region is found to be unstable only for $\alpha_{{\rm B}\phi} \leqslant -1$, and for $\alpha_{{\rm B}\phi} > -1$ a distinct instability region is located at intermediate radii. In the case f1_α0_ξ100, the pinch mode shows a growth timescale of $c\tau_{\rm I}/R_{{\rm B}\phi} \simeq 3$ at $r = 2.5R_{{\rm B}\phi}$, which is shorter than the local growth timescale for the kink mode, but longer than that for the kink mode at the central core.

ORCID iDs

José Ortuño-Macías https://orcid.org/0000-0002-9463-3137
Krzysztof Nalewajko https://orcid.org/0000-0002-2019-9438
Dmitri A. Uzdensky https://orcid.org/0000-0001-8792-6698
Mitchell C. Begelman https://orcid.org/0000-0003-0936-8488
Gregory R. Werner https://orcid.org/0000-0001-9039-9032
Alexander Y. Chen https://orcid.org/0000-0002-4738-1168
Bhupendra Mishra https://orcid.org/0000-0003-0271-3429

References

Abdo, A. A., Ackermann, M., Ajello, M., et al. 2011, Sci, 331, 739
Alves, E. P., Zrake, J., & Fiuza, F. 2018, PhRvL, 121, 245101
Alves, E. P., Zrake, J., & Fiuza, F. 2019, PhPl, 26, 072105
Appl, S., Lery, T., & Baty, H. 2000, A&A, 355, 818
Begelman, M. C. 1998, ApJ, 493, 291
Begelman, M. C., Blandford, R. D., & Rees, M. J. 1984, RvMP, 56, 255
Begelman, M. C., & Li, Z.-Y. 1994, ApJ, 426, 269
Beskin, V. S., & Nokhrina, E. E. 2006, MNRAS, 367, 375
Bodo, G., Mamatsashvili, G., Rossi, P., et al. 2013, MNRAS, 434, 3030
Bodo, G., Mamatsashvili, G., Rossi, P., et al. 2019, MNRAS, 485, 2909
Bodo, G., Mamatsashvili, G., Rossi, P., et al. 2022, MNRAS, 510, 2391
Bogovalov, S., & Tsinganos, K. 1999, MNRAS, 305, 211
Bromberg, O., & Levinson, A. 2009, ApJ, 699, 1274
Bromberg, O., Singh, C. B., Davelaar, J., et al. 2019, ApJ, 884, 39
Bromberg, O., & Tchekhovskoy, A. 2016, MNRAS, 456, 1739
Cerutti, B., Werner, G. R., Uzdensky, D. A., & Begelman, M. C. 2013, ApJ, 770, 147
Dahlin, J. T., Drake, J. F., & Swisdak, M. 2016, PhPl, 23, 120704
Das, U., & Begelman, M. C. 2019, MNRAS, 482, 2107
Davelaar, J., Philippov, A. A., Bromberg, O., et al. 2020, ApJL, 896, L31
Davis, S. W., & Tchekhovskoy, A. 2020, ARA&A, 58, 407
Drenkhahn, G., & Spruit, H. C. 2002, A&A, 391, 1141
Esirkepov, T. Z. 2001, CoPhC, 135, 144
Freidberg, J. P. 1982, RvMP, 54, 801
Giannios, D., & Spruit, H. C. 2006, A&A, 450, 887
Giannios, D., & Uzdensky, D. A. 2019, MNRAS, 484, 1378
Hillas, A. M. 1984, ARA&A, 22, 425
Istomin, Y. N., & Pariev, V. I. 1994, MNRAS, 267, 629
Kadomtsev, B. B. 1966, RvPP, 2, 153
Kirk, J. G. 2004, PhRvL, 92, 181101
Komissarov, S. S., Barkov, M. V., Vlahakis, N., et al. 2007, MNRAS, 380, 51
Komissarov, S. S., Vlahakis, N., & Königl, A. 2010, MNRAS, 407, 17
Kruskal, M., & Schwarzschild, M. 1954, RSPSA, 223, 348
Li, Z.-Y., Chiueh, T., & Begelman, M. C. 1992, ApJ, 394, 459
Lovelace, R. V. E., Newman, W. I., & Romanova, M. M. 1997, ApJ, 484, 628
Lyubarskii, Y. E. 1996, A&A, 311, 172
Lyubarskii, Y. E. 1999, MNRAS, 308, 1006
Madejski, G. M., & Sikora, M. 2016, ARA&A, 54, 725
McKinney, J. C., & Blandford, R. D. 2009, MNRAS, 394, L126
Michel, F. C. 1971, CoASP, 3, 80
Mignone, A., Rossi, P., Bodo, G., et al. 2010, MNRAS, 402, 7
Mignone, A., Striani, E., Tavani, M., et al. 2013, MNRAS, 436, 1102
Mizuno, Y., Hardee, P. E., & Nishikawa, K.-I. 2011b, ApJ, 734, 19
Mizuno, Y., Hardee, P. E., & Nishikawa, K.-I. 2014, ApJ, 784, 167
Mizuno, Y., Lyubarsky, Y., Nishikawa, K.-I., et al. 2012, ApJ, 757, 16
Mizuno, Y., Lyubarsky, Y., Nishikawa, K.-I., & Hardee, P. E. 2009, ApJ, 700, 684
Mizuno, Y., Lyubarsky, Y., Nishikawa, K.-I., & Hardee, P. E. 2011a, ApJ, 728, 90
Moll, R., Spruit, H. C., & Obergaulinger, M. 2008, A&A, 492, 621
Mukherjee, D., Bodo, G., Rossi, P., et al. 2021, MNRAS, 505, 2267
Nakamura, M., & Meier, D. L. 2004, ApJ, 617, 123
Nalewajko, K., & Begelman, M. C. 2012, MNRAS, 427, 2480
Nalewajko, K., Giannios, D., Begelman, M. C., et al. 2011, MNRAS, 413, 333
Nalewajko, K., & Sikora, M. 2009, MNRAS, 392, 1205
Nalewajko, K., Yuan, Y., & Chruślińska, M. 2018, JPlPh, 84, 755840301
Narayan, R., Igumenshchev, I. V., & Abramowicz, M. A. 2003, PASJ, 55, L69
Narayan, R., Li, J., & Tchekhovskoy, A. 2009, ApJ, 697, 1681
O'Neill, S. M., Beckwith, K., & Begelman, M. C. 2012, MNRAS, 422, 1436
Pjanka, P., & Stone, J. M. 2018, MNRAS, 477, 2376
Porth, O., & Komissarov, S. S. 2015, MNRAS, 452, 1089
Porth, O., Komissarov, S. S., & Keppens, R. 2014, MNRAS, 438, 278
Puzzoni, E., Mignone, A., & Bodo, G. 2021, MNRAS, 508, 2771
Romanova, M. M., & Lovelace, R. V. E. 1992, A&A, 262, 26
Singh, C. B., Mizuno, Y., & de Gouveia Dal Pino, E. M. 2016, ApJ, 824, 48
Sironi, L., Petropoulou, M., & Giannios, D. 2015, MNRAS, 450, 183
Spada, M., Ghisellini, G., Lazzati, D., & Celotti, A. 2001, MNRAS, 325, 1559
Tavani, M., Bulgarelli, A., Vittorini, V., et al. 2011, Sci, 331, 736
Tchekhovskoy, A., & Bromberg, O. 2016, MNRAS, 461, L46
Tchekhovskoy, A., McKinney, J. C., & Narayan, R. 2009, ApJ, 699, 1789
Tchekhovskoy, A., Narayan, R., & McKinney, J. C. 2010, NewA, 15, 749
Tomimatsu, A., Matsuoka, T., & Takahashi, M. 2001, PhRvD, 64, 123003
Uzdensky, D. A., Cerutti, B., & Begelman, M. C. 2011, ApJL, 737, L40
Vay, J.-L. 2008, PhPl, 15, 056701
Werner, G. R., Philippov, A. A., & Uzdensky, D. A. 2019, MNRAS, 482, L60
Werner, G. R., & Uzdensky, D. A. 2017, ApJL, 843, L27
Werner, G. R., & Uzdensky, D. A. 2021, JPlPh, 87, 905870613
Werner, G. R., Uzdensky, D. A., Begelman, M. C., et al. 2018, MNRAS, 473, 4840
Werner, G. R., Uzdensky, D. A., Cerutti, B., et al. 2016, ApJL, 816, L8
Yuan, Y., Nalewajko, K., Zrake, J., et al. 2016, ApJ, 828, 92
Zhdankin, V., Uzdensky, D. A., Werner, G. R., et al. 2020, MNRAS, 493, 603